Evaluation and Sensitivity Analysis of an Ocean Model Response to Hurricane Ivan

G. R. Halliwell, Jr.
MPO/RSMAS, University of Miami, Miami, Florida
(Now at: NOAA/AOML/PhOD, 4301 Rickenbacker Causeway, Miami, Florida)

L. K. Shay and J. K. Brewster
MPO/RSMAS, University of Miami, Miami, Florida

W. J. Teague
Naval Research Laboratory, Stennis Space Center, Mississippi

Submitted to Monthly Weather Review
18 May 2009

Corresponding author address: George Halliwell, NOAA/AOML.PhOD, 4301 Rickenbacker Causeway, Miami, FL, 33149,
E-mail: George.Halliwell@noaa.gov

ABSTRACT

An ocean model response to Hurricane Ivan (2004) in the northwest Caribbean Sea and Gulf of Mexico is evaluated to determine what aspects of ocean model performance need to be improved in coupled tropical cyclone forecast models. A control experiment is performed using quasi-optimal choices of initial ocean fields, atmospheric forcing fields, air-sea flux parameterizations, vertical mixing parameterization, and both horizontal and vertical resolution. Alternate experiments are conducted with one single attribute altered to quantify model sensitivity to that attribute and identify where model improvement efforts should be most effectively directed. All experiments are driven by wind stress and wind speed fields that resolve the eye and eyewall structure of the storm. Forcing that does not resolve this inner-core structure substantially degrades the ocean model response. Representation of the ocean by one-dimensional mixed layer models fails to capture important physical aspects of the ocean response that affect SST cooling and heat flux from ocean to atmosphere. Ocean model initialization with respect to the correct locations of ocean currents and eddies, and also to providing accurate upper-ocean temperature and salinity is the most important factor for insuring good ocean model performance. Next in importance are surface momentum and heat flux parameterizations. Wind stress drag coefficient parameterizations that yield values at high wind speed of 2.3-2.5 x 10^{-3} produce the most realistic wind-driven current profiles. Turbulent heat flux drag coefficient parameterizations impact heat flux from ocean to atmosphere but have little impact on SST cooling because this is dominated by entrainment at the mixed layer base. The choice of vertical mixing parameterization has a significant impact on surface heat flux from ocean to atmosphere. The impact of altering horizontal and vertical resolution is comparatively small. A horizontal resolution of ≈10 km and vertical resolution of ≈10 m in the mixed layer are adequate given that diminishing returns are encountered when either resolution is increased.

1. Introduction

Coupled ocean-atmosphere general circulation models have become increasingly important for tropical cyclone (TC) forecast guidance at operational prediction centers. Implementation and advancement of coupled TC forecast models such as the Geophysical Fluid Dynamics Laboratory (GFDL) model and more recently the Hurricane Weather Research and Forecast (HWRF) model have significantly improved track forecasts by the National Hurricane Center. However, this effort has realized little improvement in intensity forecasts, and this skill may be limited in part by errors and biases in the ocean response predicted by these coupled models.

When atmospheric conditions are favorable, TC intensification often occurs over regions with high upper-ocean heat content. This is particularly true for potentially dangerous rapid intensification. The impact of the Loop Current (LC) and warm-core anticyclones in the Gulf of Mexico (GOM) is documented for hurricanes Gilbert (1988) and Opal (1995) (Jacob *et al.*, 2000; Hong *et al.* 2000; Shay *et al.* 2000; Jacob and Shay, 2003), and also for hurricanes Katrina and Rita (2005) (Scharroo *et al.* 2005; Sun *et al.* 2006, Shay, 2008). Similar results have been obtained in the western Pacific for typhoon Maemi (2003) (Lin *et al.* 2005) and have also been obtained in statistical studies of multiple storms (Wada *et al.*, 2007; Lin *et al.,* 2008). Numerical models have reproduced the positive impact of high heat content on intensification (Schade and Emanuel, 1999; Hong *et al.* 2000; Emanuel *et al.* 2004; Lin *et al.* 2005; Wu *et al.*, 2007). In contrast, low ocean heat content can inhibit intensification; possibly contributing to the weakening of both Ivan (Walker *et al.* 2005) and Rita (Sun *et al.,* 2006; Shay 2008) as they passed over cold-core cyclones in the GOM.

To correctly forecast intensity evolution, the ocean component of coupled forecast models must accurately predict the rate and pattern of SST cooling relative to the storm center. However, ocean models have not been thoroughly evaluated for this purpose. The present study evaluates an ocean model response to Hurricane Ivan (2004) over the northwest Caribbean Sea

and GOM. Evaluation is difficult because ocean general circulation models incorporate a large suite of numerical algorithms and subgrid-scale parameterizations of processes not explicitly resolved by the model grid. Air-sea fluxes of momentum, heat, and mass (evaporation) must be parameterized. The ocean state must be accurately initialized, while the impact of the ocean outside the model domain must be provided with specified open-ocean boundary conditions. Model performance is also affected by the horizontal and vertical resolution of the grid. The relative impact of these attributes on predicting the SST response is poorly known, and it is not clear where the greatest effort toward improving model performance should be targeted. Model improvement will be difficult because errors and biases in ocean simulations arise simultaneously from all of these factors. For example, modifications of the vertical mixing parameterization that improve the upper ocean response may actually be compensating for errors and biases resulting from surface flux parameterizations. A credible model improvement effort will require a thorough understanding of how model numerics and parameterizations impact the predicted upper-ocean response to TC forcing.

The overarching goal of this analysis is to determine how we need to invest our greatest efforts toward improving ocean model performance. Sensitivity to eight individual model attributes is examined: (1) horizontal resolution, (2) vertical resolution; (3) vertical mixing and viscosity parameterizations; (4) wind stress drag coefficient parameterization; (5) turbulent heat flux drag coefficient parameterization; (6) atmospheric forcing resolution; (7) ocean model initialization; and (8) ocean dynamics (three- versus one-dimensional). Multiple experiments are performed, with one identified as the control run and the others identical to it except for altering one single attribute. Sensitivity to each attribute is quantified and their relative importance ranked without the complicating influence of atmospheric feedbacks that would be present using a coupled model. Analysis is performed on three fields based on their expected importance regarding storm intensity. In addition to the obvious choice of SST, ocean-atmosphere turbulent heat flux (latent plus sensible) averaged within specified radii of the storm center along with upper-ocean velocity profiles are considered. Heat flux is directly associated with the potential

impact of the ocean on intensity while the velocity profile is associated with the shear-driven turbulence at the ocean mixed layer (OML) base primarily responsible for SST cooling.

In addition to this sensitivity analysis, we perform a limited assessment of the overall realism of the simulated ocean response to Hurricane Ivan based on available observations, specifically an SST analysis generated from satellite and *in-situ* observations and velocity profiles obtained from moored acoustic Doppler current profiler (ADCP) measurements. Unfortunately, targeted upper-ocean aircraft observations that could have provided simultaneous measurements of temperature, salinity, and current profiles before, during, and after Ivan were not available, limiting the extent of the evaluation that could be performed.

Section 2 describes the ocean model, forcing fields, and observations. Section 3 summarizes model experiments and analysis procedures. The evaluation and sensitivity analysis is presented in the next three sections, with Section 4 focusing on SST response pattern, Section 5 emphasizing thermal fluxes from ocean to storm, and Section 6 focusing on ocean dynamics, specifically wind-driven upwelling and forced upper-ocean velocity fluctuations that are important for shear-driven OML entrainment. Conclusions are summarized in Section 7.

2. Model and Observations

a. HYCOM

The HYbrid Coordinate Ocean Model (HYCOM) is a primitive equation ocean model that uses a hybrid vertical coordinate designed to quasi-optimally resolve vertical structure throughout the ocean. This coordinate is isopycnic in the stratified ocean interior, but dynamically transitions to level coordinates near the surface to provide resolution in the surface mixed layer and to either level or terrain-following (σ) coordinates in the coastal ocean. This strategy enables HYCOM to use advanced turbulence closures for vertical mixing and also to be used as both a coastal and open-ocean model while retaining the advantages of isopycnic

coordinates in the stratified ocean interior. Model equations and initial evaluation of the hybrid vertical grid generator is presented in Bleck (2002). Subsequent evolution and further evaluation of the model is summarized in Chassignet *et al.* (2003; 2007) and Halliwell (2004).

b. Model Initialization

All experiments except one are initialized with fields provided by a data-assimilative hindcast that employs the Navy Coupled Ocean Data Assimilation (NCODA) optimum interpolation system (Cummings, 2005) to assimilate satellite altimetry and SST along with *in-situ* observations. Altimetry assimilation insures that major ocean features such as the LC and associated warm-core anticyclones and cold-core cyclones are initialized in their correct locations. This is especially important in the GOM and Caribbean Sea due to limited availability of *in-situ* observations. The NCODA system uses the Cooper and Haines (1996) algorithm to provide downward projection of anomalous temperature and salinity profiles associated with anomalous SSH. Halliwell *et al.* (2008) evaluated the same GOM NCODA hindcast product for the initialization of several storms including Ivan.

To assess sensitivity to initialization, one experiment is initialized from a non-assimilative GOM simulation where the ocean features are unconstrained by observations. Significant differences exist in the LC path and in the locations of warm-core anticyclones and cold-core cyclones between the two initialization products (Figure 1). The two cold-core cyclones present in the data-assimilative initialization (Figure 1, red arrows) that are critically important for simulating the SST response pattern forced by Ivan (Halliwell *et al.* 2008) are not present at the same locations in the non-assimilative initialization. For all experiments, the outer model product used for initialization also provides the required open-ocean boundary conditions during the runs.

c. Surface Atmospheric Forcing

Realistic atmospheric forcing fields that resolve the inner-core structure of storms are required to perform meaningful ocean model evaluation. Atmospheric or coupled ocean-atmosphere models run globally by major operational centers presently have horizontal resolution that is too coarse. The most realistic available choice is the Coupled Ocean-Atmosphere Mesoscale Prediction System (COAMPS; Hodur, 1997) with fields available at 27 km resolution. Since even this resolution is too coarse, we use the objectively-analyzed 10 m vector wind fields from the NOAA Atlantic Oceanographic and Meteorological Laboratory Hurricane Research Division (H*WIND; Powell *et al.*, 1998), to improve inner-core storm structure. These fields are produced by the objective analysis of aircraft observations combined with other available meteorological observations. Ideally, atmospheric forcing fields from a fine resolution coupled model such as HWRF should be used. However, no such product presently exists for Ivan where the storm both follows the correct path and maintains the correct intensity at all times.

Wind stress and wind speed forcing fields are generated following the procedure described in Halliwell *et al.* (2008) that blended vector wind maps from H*WIND with output from the one-degree U. S. Navy NOGAPS atmospheric model. Improved fields are generated for the present study because the H*WIND fields are blended with the higher-resolution COAMPS atmospheric model and because the H*WIND fields are now available at higher temporal resolution (three-hourly versus only at the time of research aircraft flights). The three-hourly COAMPS and H*WIND wind component fields were temporally interpolated to 30 min intervals and then blended using Eqs. (5) and (6) in Halliwell *et al.* (2008) with r_1=160 km and r_2=420 km. Thus, the vector wind fields are 100% (0%) H*WIND <160 km (>420 km) from the storm center. One realization of the blended wind speed forcing is presented in Figure 2. Vector wind stress fields are calculated from bulk formula using a prescribed drag coefficient C_D.

Other required forcing fields (air temperature, specific humidity, net radiative heat fluxes, and precipitation) are provided entirely by the COAMPS model, being horizontally interpolated to the ocean model grid points and then temporally interpolated to 30 min intervals. Surface turbulent (latent plus sensible) heat flux is calculated during model runs using bulk formula. After Ivan makes landfall, the wind speed and wind stress forcing reverts to the three-hourly COAMPS fields.

d. Observations

SST cooling patterns are evaluated against SST maps generated by the objective analysis of *in-situ* observations along with AVHRR and microwave satellite observations onto a 0.25° global grid (Reynolds *et al.*, 2002). Simulated upper-ocean velocity profiles are evaluated against moored velocity measurements. Hurricane Ivan passed directly over an array of moored ADCPs deployed by the Naval Research Laboratory over the continental shelf and slope south of Mobile, Alabama as part of the Slope to Shelf Energetics and Exchange Dynamics (SEED) project (Carnes *et al.*, 2008; Teague et al. 2006). Six shallow ADCP moorings were deployed; three each near the 60 and 90 m isobaths. Eight other ADCP moorings were deployed over the continental slope, four along the 500 m isobath and four along the 1000 m isobath near De Soto Canyon. Teague *et al.* (2007) used this dataset to study fundamental properties of the ocean response to Ivan over this shelf-slope region which represents a challenge for ocean models (e.g., transition between open-ocean and coastal regimes). Herein we evaluate model forcing at one ADCP mooring located over the continental slope of the northern GOM that was struck by the eastern eyewall of Ivan. A broader analysis over the full ADCP array is beyond the scope of this paper.

3. Experiments

Fourteen free-running HYCOM simulations were conducted to assess model sensitivity

to eight attributes (Table 1). All experiments were conducted within a domain spanning the GOM and northwest Caribbean Sea, henceforth referred to as the GOM domain, that is situated on a Mercator grid with 0.04 by 0.04cosφ degree resolution (≈4 km), where φ is latitude. The coastline follows the actual land/sea boundary but a minimum water depth of 2 m is enforced. Freshwater input from 12 rivers is included.

All experiments are referenced to a control experiment (GOM1) that has the attributes listed in the middle column of Table 1. The NCODA GOM hindcast within which it is nested was run with 20 vertical layers on the identical 0.04° mesh. The control experiment is run with 26 layers, with additional layers added to provide vertical resolution of 4-8 km in the OML (Figure 3, middle panel). The six new layers are assigned isopycnic target densities lighter than any water present within the GOM domain to force them to exist as constant-thickness layers at the top of the water column. Vertical mixing is provided by the K-Profile Parameterization (KPP) of Large *et al.* (1994) that has been modified in HYCOM to include a bottom boundary layer parameterization (Halliwell *et al.*, 2009). The vector wind stress forcing field is calculated prior to the model run using the C_D representation of Donelan *et al.* (2004). Surface turbulent heat flux and evaporation rate are calculated during the model run using the default parameterization of the latent and sensible heat flux drag coefficients C_{EL} and C_{ES}, specifically the COARE 2.6 algorithm (Fairall *et al.*, 1996; Andreas and DeCosmo, 2002). Model fields are initialized on 0000 UTC, 10 September 2004 and the simulation is run for three weeks.

The remaining experiments (GOM2-GOM14) each differ from GOM1 by altering the single model attribute listed in Table 1. The alternate horizontal resolution experiment GOM2 is run in the same domain, but on a 0.08° Mercator mesh consisting of every other point of the control grid. Two alternate vertical resolutions are tested, one coarser (21 layers, GOM3) and one finer (31 layers, GOM4) than the control experiment (Figure 3; Table 1), requiring one and eleven additional layers to be added respectively. Two alternate vertical mixing parameterizations are evaluated: the Mellor-Yamada (MY) level 2.5 turbulence closure (Mellor and Yamada, 1982) in GOM5 and the Goddard Institute for Space Studies (GISS) level 2

turbulence closure (Canuto *et al.*, 2001; 2002) in GOM6. Experiments GOM7-GOM10 use the algorithms of Powell *et al.* (2003), Large and Pond (1981), Large and Pond with C_D capped at a constant value above 30 m s^{-1}, and Shay and Jacob (2006). These parameterizations are graphed in Figure 4. One alternate representation of C_{EL} and C_{ES} is used in GOM11, specifically the Kara *et al.* (2002) algorithm. Coefficients from both algorithms are graphed in Figure 4 for a representative choice of air temperature and SST. Experiment GOM12 evaluates sensitivity to atmospheric forcing resolution by using COAMPS forcing alone. GOM13 is nested in the non-assimilative outer model to evaluate sensitivity to initialization. Finally, GOM14 uses the HYCOM code configured to run as a one-dimensional ocean model to demonstrate the importance of three-dimensional ocean dynamics. In this experiment the ocean is represented by a set of independent one-dimensional mixed layer models (KPP diffusion and viscosity with a one-dimensional momentum balance) at each grid point.

4. SST Cooling

a. Results from the Control Experiment

The control simulation is run with the same model parameterizations as the experiment analyzed by Halliwell *et al.* (2008) to document the impact of ocean model initialization. However, improved comparison between model and observations is expected because of: (1) improved blended forcing; (2) several upgrades to the model code; and (3) the use of a more optimal SST analysis for model evaluation. As in the earlier study, post-storm SST cooling in the control experiment is largest within the two cold-core cyclones initially present in the eastern GOM (Figures 1, 5). The comparison of model results to an SST analysis derived solely from microwave satellite measurements performed by Halliwell *et al.* (2008) demonstrated that the model substantially overcooled within both cyclones. However, post-Ivan AVHRR images analyzed by Walker *et al.* (2005) suggested that the daily microwave SST analysis may have

underestimated the actual cooling that occurred within these cyclones. The inclusion of AVHRR and *in-situ* measurements in the Reynolds SST analysis used herein produced colder post-Ivan SST within these features, by ≈2°C in the northern cyclone and ≈1°C in the southern cyclone. With this change, the control experiment overcooled with respect to the SST analysis by only 0.6° in the northern cyclone (Table 2). However, it still excessively overcooled by 4.3°C in the southern cyclone. Because the simulated cooling over the remainder of the eastern GOM and northwest Caribbean Sea is generally close to the observed magnitude (Figure 5), the control experiment produced realistic SST cooling everywhere except in the southern cyclone.

The impact of ocean features on the cooling pattern is explored further by graphing temperature as a function of time and depth at the two locations illustrated in Figure 5, top panel: one located at the eastern end of the detached warm anticyclone and the other located near the center of the southern cold-core cyclone. Both points are located about 45 km, or one radius of maximum wind speed (R_{MAX}), east of the track with R_{MAX} estimated from the blended wind speed forcing field (Figure 2). This is the approximate location relative to the track where the largest near-inertial currents are forced (e.g. Sanford *et al.*, 2007). These profiles are calculated during model runs by inserting synthetic moorings at these two locations with instruments deployed at 5 m vertical intervals. Model fields are sampled at each synthetic instrument using two-dimensional polynomial horizontal interpolation to the mooring locations and then performing linear vertical interpolation to instrument depths.

SST cooling is larger within the cyclone (10°C) compared to the anticyclone (3°C) because of both the thinner initial surface warm layer and the stronger wind-driven upwelling (Figure 6). To highlight the contribution of upwelling, terms of the OML thickness balance are estimated:

$$w_E = w_M - \frac{\partial z_M}{\partial t}, \tag{1}$$

where w_E is entrainment velocity and w_M is the vertical velocity at the depth of the OML base z_M. The two terms on the right side are diagnosed from the model output, and then w_E is estimated as

a residual. The OML base is diagnosed as the depth where temperature is 0.5°C colder than the surface (layer 1) temperature. Vertical velocity is diagnosed during model runs at the central depth of each model layer at each grid point using the procedure presented in Halliwell *et al.* (2003). It is then horizontally interpolated to the synthetic mooring locations using two-dimensional polynomial interpolation and then vertically interpolated to the OML base using linear interpolation.

These three terms reveal large differences in the OML depth balance between the warm ring and cold cyclone (Figure 6). Prior to the time the eye passes the warm ring location, w_M is small so that $w_E \approx -\partial z_M/\partial t$, indicating that upwelling makes little contribution to the cooling. After the storm passes, OML penetration abruptly ceases as w_M gradually increases, peaking about 0.2 inertial periods (IP) or about 5 hr after passage and then remaining positive through 0.4 IP. During this time interval, w_E is small or negative (detrainment) and upwelling still has little impact on cooling. In contrast, upwelling in the cold cyclone makes a substantial contribution to cooling both prior to and during storm passage, with w_E peaking at the time of passage and remaining positive for about 0.25 IP thereafter. The rate of OML deepening is small for about 0.2 IP prior to passage so that $w_E \approx w_M$, During this time interval, the upwelling increases cooling by lifting colder water toward the OML base and by maintaining a thinner OML, with the latter impact resulting in increased OML entrainment by both wind-forced TKE and shear instability of the wind-driven horizontal flow at the OML base. Following storm passage, entrainment rapidly weakens and the upwelling primarily acts to raise the OML base. Beginning around 0.2 IP after passage when w_M is small, the weak stratification remaining at the OML base permits rapid OML deepening due to large entrainment driven by the shear of the near-inertial current fluctuations. Entrainment cooling remains significant until 0.5 IP after passage and maximum cooling is realized about 0.4 IP (10 hr) after passage.

Further insight on the impact of upwelling and other aspects of three-dimensional ocean dynamics is obtained by comparing the time-depth temperature and vertical velocity plots from the one-dimensional experiment GOM14 to those from the control experiment at the same two

locations (Figure 6). Without wind-driven vertical velocity in both the anticyclone and cyclone, w_E is large prior to and during passage, but then decreases rapidly within 0.1 IP after passage as wind forcing relaxes and the OML approaches its maximum thickness. SST cooling produced by GOM14 is smaller compared to the control, 2°C versus 3°C in the anticyclone and 5°C versus 10°C in the cyclone (Figure 6). As discussed earlier, wind-driven vertical velocity is a major contributor to increased cooling in the cyclone. The story is different in the anticyclone because the warm layer present 0.5 IP before the storm in GOM14 is thinner than in the control experiment, a situation that likely contributed substantially to the increased cooling. The different warm layer thicknesses occur because the measurement point is located at the eastern edge of the anticyclone and the warm layer there becomes thinner over the first few days of the simulation as this feature propagates westward. This analysis demonstrates the critical importance of ocean dynamics not only because wind-driven upwelling can contribute significantly to SST cooling, but also because the upwelling pattern can be highly distorted by the background vorticity field associated with pre-existing ocean features (Jaimes and Shay, 2009a; 2009b).

The excess cooling produced by the control experiment in the southern cyclone is too large to blame on errors and biases in the SST analysis. To determine if model initialization could have been a factor, the ocean heat content (OHC; Leipper and Volgenau, 1972) referenced to the 26°C isotherm depth (D_{26}) derived from satellite altimetry, SST measurements, and ocean climatology (Mainelli *et al.*, 2008) is compared to values calculated from initial model fields. Values for the southern cyclone are estimated over a 1° by 1° box centered at 86.8°W, 25.0°N. The derived OHC (D_{26}) value is 40 kJ cm^{-2} (48 m) while the initial model values are 25 kJ cm^{-2} (32 m). This initial cold bias may therefore have contributed to the overcooling. However, the detailed horizontal and vertical structure of ocean features provided by the initialization may also have influenced the upwelling pattern and its impact on cooling. Although it is possible that the vertical mixing parameterization could contribute to the overcooling, separating this contribution from others will be difficult. Future efforts to improve ocean model performance will depend

heavily on the availability on detailed, high-quality, three-dimensional ocean observations before, during, and after individual storms to identify and separate the contributions of these different factors.

b. Sensitivity to Model Attributes

Sensitivity of the SST cooling pattern is evaluated by comparing SST changes from experiments GOM2 through GOM14 to those from the control experiment GOM1. SST change is calculated for the control experiment as $\Delta T_C = (T_2 - T_1)_C$ and for each alternate experiment as $\Delta T_A = (T_2 - T_1)_A$, where T_1 (T_2) is SST before (after) Ivan. The difference in SST change between each alternate experiment and the control experiment given by

$$\Delta T = \Delta T_A - \Delta T_C \tag{2}$$

is analyzed in Figure 7, where the tabulated RMS amplitude of ΔT quantifies the similarity of each alternate experiment to the control experiment. Inset maps of ΔT are also presented in Figure 7 for four of the alternate experiments. All statistics are calculated within the region outlined by the box in these four maps which covers the eastern GOM and extreme northwest Caribbean Sea.

The simulated SST response is most sensitive to the alternate initialization (GOM13) with an RMS ΔT of 1.57°C. This large amplitude is evident in the inset map (Figure 7). Large positive ΔT exists at the locations of the two cold-core cyclones because these features were not present in the alternate initialization. Substantial sensitivity to initialization extends beyond these ocean features and also beyond the region directly forced by the storm. Ocean model sensitivity to initialization is therefore likely to remain significant over other ocean regions with less energetic features. Even in the absence of energetic ocean features, it is still necessary to accurately initialize temperature and salinity structure. The next largest sensitivity is observed for ocean dynamics (GOM14) with an RMS ΔT of 1.31°C. At the other extreme, SST response is least sensitive to vertical resolution (RMS ΔT of 0.29°C for low resolution and 0.26°C for high

resolution), and also to turbulent heat flux drag coefficients (RMS ΔT of 0.18°C). The latter lack of sensitivity exists despite differences of ≈30-40% in values of C_{EL} and C_{ES} (Figure 4). Although surface heat flux is expected to be sensitive to these different coefficient values (Section 5), it has a relatively small influence on SST cooling which mostly arises from entrainment across the OML base.

Intermediate ocean model sensitivity exists to the remaining attributes of horizontal resolution, vertical mixing, wind stress drag coefficient, and atmospheric forcing resolution. The exception to this is the small RMS ΔT value of 0.19°C realized for the Large & Pond C_D capped at high wind speed, which produced very similar C_D values to those of Donelan used in the control experiment (Figure 4). The inset ΔT map for GOM6 (GISS vertical mixing) along with the mean ΔT difference of 0.21°C (Figure 7) demonstrates that this mixing scheme produces less SST cooling than KPP. The same is true for MY mixing (not shown). Parameterizations of C_D that produce larger (smaller) values result in greater (less) SST cooling. The inset map for GOM8 (Large and Pond C_D) reveals the enhanced SST cooling produced by this experiment (Figure 7). The same is true for GOM10 (Shay and Jacob C_D) while the opposite is true (reduced cooling compared to control) for GOM7 (Powell C_D). This relationship results from differences in the strength of wind-driven turbulence resulting from changes in surface friction velocity, and also from changes in the magnitude of wind-driven flow impacts both upwelling and shear at the OML base.

A Taylor (2001) diagram (Figure 8) is also used to compare ΔT_A from each alternate experiment to ΔT_C. To construct this diagram, the mean is first removed from each ΔT_A and ΔT_C map, and then all maps are normalized by the variance of ΔT_C. This diagram is effective because it simultaneously represents three different metrics by a single point. The large black square in the diagram is the point that signifies a perfect comparison (correlation coefficient of 1.0, identical normalized RMS amplitude of 1.0, and RMS difference of zero between maps). One plotted point quantifies the similarity between ΔT_A and ΔT_C, with the RMS amplitude of ΔT_A given by radial distance from the plot origin at the lower left corner, RMS difference between the

two fields being proportional to linear distance between the plotted point and the large black square, and correlation coefficient being a function of the direction angle of the vector connecting the plot origin with the plotted point (Figure 8).

The greatest sensitivity again results from the alternate initialization (GOM13) which has a (correlation, normalized RMS amplitude, normalized RMS difference) of (0.59, 0.58, 0.81) with respect to the control experiment (Figure 8). The small RMS amplitude of 0.58 is due largely to the absence of the two cyclones directly hit by Ivan and the associated large cooling. The one-dimensional experiment (GOM14) has a (correlation, RMS amplitude, RMS difference) of (0.72, 0.97, 0.72) with the control experiment. All other alternate experiments are highly correlated with the control experiment (≥0.95, Figure 8) demonstrating that correct model initialization and three-dimensional ocean dynamics are necessary to accurately predict the SST response. At the other extreme, the two experiments displaying the least SST sensitivity are GOM11 (alternate turbulent heat flux parameterization) and GOM9 (Large and Pond C_D capped at high wind speed to values close to the Donelan *et al.* (2004) parameterization). The dependence of RMS amplitude on C_D is evident as is the several-percent reduction in RMS amplitude produced by the two alternate vertical mixing choices. RMS amplitude produced by GOM12 (no H*WIND blending) is reduced by ≈25% due to the highly smoothed representation of inner-core storm structure and the resulting reduction in maximum wind speed.

Since these comparisons are substantially influenced by the large cooling that occurred within the two cyclones, the focus now shifts to the cooling that occurred in these features (Table 2). The largest underestimate of cooling relative to the control experiment is produced by GOM13 within the southern cyclone where post-Ivan SST is 6.9°C warmer than in GOM1 because of the absence of this feature. The inadequate resolution of storm structure by the alternate forcing (GOM12) and the absence of three-dimensional ocean dynamics (GOM14) each led to reduced cooling of 1.0-3.2°C in both cyclones (Table 2). Little difference in cooling results from altering horizontal and vertical resolution or from altering turbulent heat flux drag coefficients. The two alternate vertical mixing choices reduce SST cooling relative to control by

0.6-1.8°C while C_D parameterizations that produce larger (smaller) values than the Donelan *et al.* (2004) choice increase (decrease) the cooling by up to 0.9°C (1.5°C).

c. Evaluation against SST Analysis Maps

To evaluate the realism of the SST cooling pattern from all experiments against observations, a Taylor diagram analysis compares ΔT_A and ΔT_C maps from all 14 experiments to ΔT_R maps calculated from the Reynolds SST analysis. In this case, all maps are normalized by the variance of the ΔT_R map. This evaluation is supplemented by analysis of the Murphy (1988) skill score S, given by:

$$S = r^2 - \left[r - \left(\frac{\sigma_Y}{\sigma_X} \right) \right]^2 - \left[\left(\frac{\bar{Y} - \bar{X}}{\sigma_X} \right) \right]^2, \quad (3)$$

Where $\bar{X}$ and $\bar{Y}$ are the mean values of fields X and Y, σ_X and σ_Y are their standard deviations, and r is the correlation coefficient between them. If the two maps have the same mean and standard deviations, then $S=r^2$; otherwise, $S < r^2$. Values exceeding zero represent statistically significant skill. Skill score supplements the Taylor diagram analysis which only quantifies the difference in structure between fields and not the mean difference.

In the Taylor diagram (Figure 9), the control experiment has a (correlation, normalized RMS amplitude, normalized RMS difference) of (0.71, 1.20, 0.86). The resulting skill score S=0.21 (Table 3) is significant but not large due to the 20% amplitude overestimate and RMS difference values that are nearly as large as the RMS amplitudes of the two maps. Eleven of the fourteen experiments produce correlation coefficients between 0.67 and 0.72, and the different model attributes primarily influence normalized RMS amplitudes. The dependence of RMS amplitude on the value of C_D is particularly evident. The two experiments using the largest values of C_D (GOM8, GOM10) produced insignificant (negative) values of S. Of the remaining three experiments, the alternate initialization experiment GOM13 is the largest outlier, with (correlation, normalized RMS amplitude, normalized RMS difference) of (0.41, 0.66, 0.97) and

insignificant *S*. The alternate forcing experiment GOM12 produces substantially smaller normalized RMS amplitude (0.88) than most other experiments along with a slightly reduced correlation of 0.65 and insignificant *S*. One dimensional dynamics (GOM14) results primarily in a modest reduction in correlation to 0.61 but with a very small S=0.01. Overall, the experiments overestimate the amplitude of the SST change pattern forced by Ivan by ≈20% compared to the Reynolds analysis, which probably results to a large extent from the overcooling in the southern cyclone.

5. Thermal Energy Provided by the Ocean to the Storm

a. Estimation Procedure

Although the accuracy of SST forecasts are important, it is the thermal energy provided by the ocean to the storm that most directly impacts TC intensity. To perform a sensitivity analysis of this flux to model attributes, the surface turbulent heat flux is averaged within a specified radius of the storm center and graphed along the storm path. The choice of averaging radius is important because it should include the area of the ocean surface that is actually providing the large majority of thermal energy to the storm. Since this choice is uncertain (e.g. Shen *et al.*, 2002), sensitivity analysis is performed for two different radii: $1.4R_{MAX}$ and $3R_{MAX}$, where R_{MAX} is the radius of maximum wind. These choices are illustrated on the blended wind speed forcing map (Figure 2) where $1.4R_{MAX}$ encloses the region influenced by the eye and eyewall while $3R_{MAX}$ roughly encloses most of the region influenced by hurricane force winds. Surface turbulent heat flux Q_T averaged over these two radii is graphed as a function of storm latitude for all experiments in Figure 10. Without atmospheric feedback, differences in the averaged heat fluxes depend primarily on differences in SST cooling rate over the averaging domain. Although this type of sensitivity analysis is most appropriately performed with a coupled model that produces atmospheric feedback, it is still important to understand how ocean

model attributes alone influence the oceanic contribution to surface turbulent heat flux.

b. Sensitivity Analysis

The progression of mean Q_T along the storm path in the control experiment is strongly influenced by the oceanographic features. Over the northwest Caribbean and the LC (south of 23°N), mean Q_T within $1.4R_{MAX}$ of the storm center averages about -600 W m^{-2}. When the storm encounters the two cyclones, SST cooling inside the averaging radius is sufficiently rapid to produce positive turbulent (sensible only) heat flux from atmosphere to ocean as SST becomes colder than air temperature. This impact of the cyclones is likely exaggerated because air temperature is provided by the COAMPS atmospheric model and atmospheric feedback cannot occur. The overcooling by the model also contributes to this flux reversal. Some atmospheric feedback is present in the COAMPS air temperature forcing since it was coupled to an ocean model, but the air temperature probably remains too high because the coarse representation of Ivan in the COAMPS atmospheric model probably produced insufficient SST cooling in the coupled model run. Experiment GOM12 (no H*WIND blending) is consistent with this hypothesis since it underestimated SST cooling in the cold-core cyclones by ≥2°C (Table 2). Despite this exaggerated flux reversal, it remains clear that thermal energy provided by the ocean to the inner-core region of the storm is very sensitive to the presence of these warm and cold ocean features. The progression of Q_T over the larger $3R_{MAX}$ averaging region is similar over the northwest Caribbean and the LC, but the change in Q_T as the storm passes over the two cyclones is substantially reduced because warmer water outside of the cyclones is included in the averaging region. The flux is near zero over the southern cyclone and remains negative (ocean to atmosphere) over the northern one.

Little sensitivity of Q_T to either horizontal or vertical grid resolution exists for both averaging radii (Figure 10a, b), but substantial sensitivity exists for all other model attributes. Focusing on the $1.4R_{MAX}$ averaging area, altering the vertical mixing algorithm produces

differences up to 200 W m^{-2} (20-30%) over the northwest Caribbean and LC (Figure 10c). Altering either the wind stress or turbulent heat flux drag coefficients produces larger differences of up to 300 W m^{-2} (30-40%) for C_D (Figure 10e) and 250 W m^{-2} (20-30%) for C_{EL} and C_{ES} (Figure 10g). Although large heat flux sensitivity to changes in C_{EL} and C_{ES} does exist, SST is not sensitive since surface heat flux does not make a leading order contribution to SST change. Large sensitivity is also observed as expected for both the low-resolution forcing and the alternate model initialization experiments (Figure 10i), the latter particularly affected by the absence of the southern cyclone. Except for turbulent flux drag coefficients, changes in model attributes that cool SST faster produce reduced heat loss to the atmosphere as expected.

Sensitivity results are generally similar over the larger $3R_{MAX}$ averaging radius. However, over the northwest Caribbean and LC, the differences that result from altering vertical mixing and wind stress drag coefficient are smaller than the differences over the smaller averaging radius (Figure 10d, f). The sensitivity of surface heat flux to altering these two model attributes is greatest in the inner core region of the storm.

6. Ocean Dynamics

a. Sensitivity of Vertical Velocity to Model Attributes

Given that vertical advection can contribute significantly to SST cooling, sensitivity of vertical advection to changes in model attributes is assessed by graphing vertrical velocity *w* at 50 m depth as a function of time (Figure 11) at the same two locations (warm anticyclone and southern cyclone) where the impact of vertical velocity on SST cooling was analyzed in Figure 6. The only difference is that *w* estimates at sampled by the synthetic instruments are vertically interpolated to 50 m instead of the OML base. The behavior of *w* in the control experiment is consistent with the results summarized in Figure 6, with maximum positive *w* occurring near the time of storm passage in the southern cyclone and with somewhat weaker maximum positive *w*

lagging storm passage by a few hours in the eastern part of the warm anticyclone. The least sensitivity of w is to altered vertical resolution. Although sensitivity to horizontal resolution in the warm ring is also small, the peak in maximum w is smoother with maximum value reduced by ≈25%. Little sensitivity is evident when C_{EL} and C_{ES} are changed as expected. When other model attributes are altered, maximum w can vary by 50% or more in the southern cyclone. This sensitivity is sufficiently large that differences in the three-dimensional flow response beneath the inner core of the storm probably contribute to differences in the SST cooling there. In contrast, substantially less sensitivity is observed in the warm ring for all model attributes.

b. Velocity Profiles Produced by the Control Experiment

ADCP observations from SEED mooring 9 are used to evaluate the capability of the control experiment to simulate the wind-driven near-inertial current response (Teague *et al.*, 2007), which is critically important to shear-driven turbulent entrainment at the OML base. The u and v components at this mooring are shown for the upper 150 m of the water column over a time interval ranging from 0.5 IP before the storm to 1.5 IP after passage which represents the forced response and the subsequent transition to unforced near-inertial wave variability very (Figure 12). Observed velocity components are graphed over the same time-depth range except for the upper 40 m where the ADCP could not sample velocity. The response is dominated by forced, near-inertial waves, and the simulated response closely resembles the observed response over their common depth range. These observations and simulations suggest that vertical energy propagates out of the surface mixed layer and into the thermocline in a manner consistent with theory. Westward mean flow is present in the u field while mean v is near zero. This close resemblance between observations and simulations is encouraging.

c. Sensitivity of Velocity Profiles to Model Attributes

A Taylor diagram is used to quantify sensitivity by comparing *v* fields from each alternate experiment to *v* generated by the control experiment (Figure 13). To construct this diagram, the mean was first removed from each *v* field over the time interval between -0.5 and 1.5 IP and over the upper 150 m. The resulting two dimensional fields were normalized by the variance of the field from the control experiment. In contrast to the situation farther offshore, the alternate initialization (GOM13) is not an outlier for simulated velocity. The initial flow at SEED mooring 9 is westward in both GOM13 and GOM1 (Figure 12), so the different initializations produced similar background flow in this region.

The greatest outliers in the sensitivity analysis are the low-resolution atmospheric forcing experiment GOM12 and the one-dimensional experiment GOM14. GOM12 underestimates velocity amplitude by 40% relative to the control and correlation with the control is reduced to 0.9, the latter resulting primarily because the weaker forced currents do not penetrate as deep into the water column (not shown). GOM14 overestimates amplitude by >40% and produces a substantial reduction in correlation to 0.66 because the response is purely inertial and energy does not penetrate into the ocean interior through near-inertial wave dynamics (not shown). That is, the frequency of the oscillations is at the local IP which means no vertical energy propagation (Shay and Elsberry 1987; Shay et al., 1989). The correlation is also reduced because GOM14 produces current fluctuations with exactly inertial period while GOM1 produces fluctuations with a period about 10% smaller than inertial (Figure 12).

The next greatest level of sensitivity results from altering wind stress drag coefficient. The choices that produce larger (smaller) C_D values produce larger (smaller) RMS amplitudes than the control experiment. Both increased and decreased C_D is associated with a reduction in correlation, primarily because increased (decreased) C_D is associated with increased (decreased) penetration of the wind-forced currents deeper into the water column (not shown). One choice of C_D (Large and Pond capped, GOM9) displays little difference from the control experiment since C_D values are very close to the Donelan *et al.* (2004) choice used for the control (Figure 4). These results are generally consistent with simulations of the ocean response to Hurricane

Francis (2004) by Sanford *et al.* (2007) who determined that runs with C_D values capped or reduced at high wind speeds outperformed runs using the uncapped Large and Pond representation. Small sensitivity is observed to altering vertical mixing choice and both vertical and horizontal resolution. The alternate heat flux coefficient experiment produces fluctuations that are nearly identical to the control experiment as expected.

c. Evaluation of Velocity Profiles against Observations

Taylor diagram analysis is performed to compare *v* fluctuations at SEED mooring 9 produced by all 14 experiments to the observed fluctuations (Figure 14). It is conducted over the common depth range of 40 to 150 m and from 0.5 IP before to 1.5 IP after the storm. All fields are normalized by the variance of the observed *v* fluctuations. The control experiment produces one of the most realistic simulations of upper-ocean *v* fluctuations with (correlation, normalized RMS amplitude, normalized RMS difference) of (0.89, 1.46, 0.48). Horizontal resolution, turbulent heat flux drag coefficient, and the capped Large and Pond wind stress drag coefficient all have a minor influence on the quality of the response while horizontal resolution has only a slightly larger influence.

Vertical mixing choice has a substantial influence on magnitude, with both the MY and GISS experiments (GOM5 and GOM6) producing a substantially weaker velocity response. This result contrasts with the sensitivity evaluation in Figure 13 where the other vertical mixing choices produced velocity fluctuations of similar magnitude to the control experiment. This difference occurred because the present comparison to observations is limited to the depth range 40 and 150 m, suggesting that the forced velocity fluctuations in GOM5 and GOM6 are more surface intensified and do not penetrate downward into the water column as effectively as they do in the control experiment. Consequently, the KPP mixing choice produces the most realistic response with respect to these observations.

The choice of wind stress drag coefficient has a significant influence, with the choice of

Large and Pond capped at high wind speed producing velocity fluctuations that were as realistic as the control experiment due to values of C_D very similar to the Donelan *et al.* (2004) choice (Figure 4). The other choices of C_D that produced larger or smaller values degraded the overall realism of the simulated velocity fluctuations. The two most unrealistic simulations (GOM12 and GOM14) were poorly correlated with the observations. The attribute choices for the control are quasi-optimal for reproducing the upper-ocean velocity response at this location. In particular, wind stress drag coefficient choices that are capped at values between 2.3×10^{-3} and 2.5×10^{-3} produce velocity fluctuations very close to the observed amplitude and with realistic vertical structure. Parameterizations that continue to increase in value with wind speed at high values are comparatively less realistic in agreement with Sanford *et al.* (2007).

7. Conclusions

.

The response of an ocean model to TC forcing, specifically Hurricane Ivan (2004), has been documented in the GOM and NW Caribbean Sea. The sensitivity of the simulated response to changes in several specific attributes of the model (Table 1) was quantified and the realism of the model response was evaluated against SST images derived from satellite and *in-situ* measurements along with upper-ocean current profiles measured at an ADCP mooring. Key results are summarized in Table 4 along with recommendations for each model attribute. In drawing conclusions from these results, it must be kept in mind that they are representative of one particular storm in one distinct ocean region, and have been obtained from a standalone ocean model without atmospheric feedback that was driven by quasi-optimal but imperfect atmospheric forcing. Despite these limitations, the present study represents a baseline effort to understand the strengths and limitations of ocean models with respect to their numerics and parameterizations, a first step toward the ultimate goal of improving their performance in coupled forecast models. It provides guidance toward where we should most effectively invest our efforts to improve model performance.

Representation of the ocean by one-dimensional mixed layer models is inadequate for predicting the ocean response to many storms. Energetic ocean features such as the LC, rings, and eddies in the GOM distort the wind-driven momentum response and associated upwelling patterns that can significantly influence SST cooling beneath a storm (e.g. Jaimes and Shay, 2009a; 2009b). This impact was particularly evident between the detaching warm anticyclone and a cold-core cyclone present just to the southeast of this ring where upwelling was enhanced within the cyclone. However, one-dimensional mixed layer models predict a purely inertial response without upwelling that is slowly damped by friction. Furthermore, the absence of near-inertial wave dynamics precludes the downward dispersion of near-inertial wave energy out of the OML into the ocean interior. The absence of horizontal heat advection is also a potentially important issue that has not been considered here, particularly for slower-moving storms passing over a western boundary current such as the LC (Shay and Uhlhorn 2008). Neglecting the three dimensional response becomes even more important when a second storm (Isidore and Lili 2002; Katrina and Rita 2005; Gustav and Ike 2008) follows similar tracks and can potentially lead to larger forecast errors in coupled models. The urge to design efficient coupled forecast models containing a one-dimensional ocean should be resisted.

Existing operational atmospheric models are run at a horizontal resolution too coarse to resolve the inner-core TC structure. For this reason, the H*WIND wind analysis was blended into fields from the U. S. Navy COAMPS atmospheric model to generate forcing for the control experiment in this study that at least marginally resolved the horizontal scales of the eye and eyewall. An alternate experiment forced by the COAMPS model alone substantially degraded the quality of the simulated ocean response. Research studies of the ocean response to a TC should not use forcing fields from these existing operational atmospheric models. The question of whether the scales resolved by H*WIND are fully adequate could not be addressed here because higher-resolution forcing from an atmospheric model that accurately resolved both the track and intensity of Ivan was not available. Since operational forecast centers are moving toward using nested atmospheric models with resolution of O(1 km), atmospheric model

resolution should not be an issue for coupled TC forecast models in the future.

The most important issue for insuring accurate performance of a three-dimensional ocean model forced by a TC is to accurately initialize the ocean fields. The two important aspects of initialization are ocean feature location and providing accurate profiles of temperature, salinity, and density within the existing features. The latter issue remains important even in relatively quiescent ocean regions. The control experiment was initialized from a data-assimilative ocean hindcast where the LC, a detaching warm ring, and two associated cold-core cyclones that had a large impact on the final SST cooling pattern were correctly situated. An alternate experiment initialized from a non-assimilative ocean model demonstrated that feature location had a much larger influence on the responses of SST, wind-driven upwelling, and heat flux from ocean to atmosphere than did other model and air-sea flux parameterizations. Although this study was conducted in a region where water mass and heat content differences between ocean features are large, the impact on model performance within the GOM was so large that feature initialization will likely remain of leading order importance in all tropical/subtropical ocean regions containing mesoscale ocean variability. The second aspect of initialization, the upper-ocean thermal and baroclinic current structure within ocean features, still poses significant problems (Halliwell *et al.*, 2008) that will extend to all ocean regions. An apparent initial cold bias in the southern cold-core cyclone may have contributed to overcooling in this feature by the control experiment although contributions from upwelling and the vertical mixing parameterization could also have been significant.

Air-sea flux parameterizations have an intermediate to high impact on all important aspects of model sensitivity (Table 4). For wind stress, the magnitude of C_D at high wind speeds impacts SST cooling and heat flux from ocean to atmosphere by (1) modifying the rate of OML deepening by wind-driven turbulence (friction velocity); and (2) altering the magnitude and three-dimensional structure of wind-driven currents and wind-driven upwelling. For turbulent heat flux, an alternate experiment using a parameterization of C_{EL} and C_{ES} that produced values 20-40% higher that the one used in the control experiment (Figure 4) had a large influence on the

turbulent heat flux as expected, but had very little impact on SST cooling since entrainment at the OML base makes the dominant contribution to this cooling. Substantial effort will have to be directed toward verifying parameterizations of surface flux drag coefficients in coupled TC forecast models.

Although the SST response displayed intermediate sensitivity to the three vertical mixing models tested, both wind-driven upwelling and air-sea heat flux displayed high sensitivity comparable to the sensitivity of surface flux drag coefficients. Although a substantial effort to improve the performance of vertical mixing models is warranted, further improvement in model initialization and surface flux parameterizations will first be necessary; otherwise, vertical mixing may be "tuned" to correct for errors and biases resulting from these other factors.

Horizontal resolution has low to intermediate influence on all important aspects of model performance (Table 4). Although it has intermediate impact on SST cooling, it has small influence on the heat flux from ocean to atmosphere. This probably results in part because much of the RMS difference occurs at small scales since the higher-resolution experiment provides a sharper resolution of temperature changes across fronts. As a result, these SST differences have only a small impact on area-integrated heat flux. Sensitivity to vertical resolution is low with respect to all important aspects of model performance. Given the greater sensitivity to other model attributes, there is no need to invest a lot of effort to optimize model horizontal or vertical resolution. Based on the Ivan results, ocean models run at horizontal resolution of $\leq$10 km and a vertical resolution within the OML of $\leq$10 m will be adequate for addressing the greater concerns enumerated above.

These results represent an early, yet important step toward improving the performance of the ocean component of coupled forecast models. Ocean model studies must be extended to other storms and other ocean regions, while evaluation and sensitivity analysis of coupled forecast models must also be performed. This will require an ongoing observational effort to insure that high-quality observations of currents and baroclinic structure with sufficient detail and both three-dimensional and temporal coverage exist to perform the detailed evaluation studies

required to formulate effective model improvement strategies.

Acknowledgments.

This work was sponsored by the National Oceanic and Atmospheric Administration (grant number NA17RJ1226) and the National Science Foundation (grant number ATM0444525). The Reynolds SST maps were obtained from http://www.ssmi.com. The Office of Naval Research supported the Naval Research Laboratory's basic research project "Slope to Shelf Energetics and Exchange Dynamics" (SEED) under Program Element 0601153N.

References

Andreas, E. L, and J. DeCosmo, 2002: The signature of sea spray in the HEXOS turbulent heat flux data. *Bound.-Layer Meteor.*, **103**, 303–333.

Bleck, R., 2002: An oceanic general circulation framed in hybrid isopycnic-Cartesian coordinates., *Ocean Modelling*, 4, 55-88.

Canuto, V. M., A. Howard, Y. Cheng, and M. S. Dubovikov, 2001: Ocean turbulence. Part I: One-point closure model-momentum and heat vertical diffusivities. J. Phys. Oceanogr., 31, 1413-1426.

Canuto, V. M., A. Howard, Y. Cheng, and M. S. Dubovikov, 2002: Ocean turbulence. Part II: Vertical diffusivities of momentum, heat, salt, mass, and passive scalars, *J. Phys. Oceanogr*., 32, 240-264.

Carnes, M. R., W. J. Teague, and E. Jarosz, 2008: Low-frequency current variability observed at the shelfbreak in the northeastern Gulf of Mexico: November 2004 - May 2005, *Cont. Shelf Res*., **28**, 399-423.

Chassignet, E. P., L. T. Smith, G. R. Halliwell, and R. Bleck, 2003: North Atlantic simulation with the HYbrid Coordinate Ocean Model (HYCOM): Impact of the vertical coordinate choice, reference density, and thermobaricity. *J. Phys. Oceanogr.*, **33**, 2504-2526.

Chassignet, E. P., H. E. Hurlburt, O. M. Smedstad G. R. Halliwell, P.J. Hogan, A. J. Wallcraft and R. Bleck, 2007: The HYCOM (Hybrid Coordinate Ocean Model) data assimilative system. *J. Mar. Sys*., **65**, 60-83.

Cione, J. J. and E. W. Uhlhorn, 2003: Sea surface temperature variability in hurricanes: implications with respect to intensity change. *Mon. Wea. Rev.*, **131**, 1783-1795.

Cooper, M. and K. Haines, 1996: Altimetric assimilation with water property conservation. *J. Geophys. Res*., **101**, 1059-1078.

Cummings, J. A., 2005: Operational multivariate ocean data assimilation. *Quart. J. Royal Met. Soc*., **131**, 3583-3604.

D'Asaro, E. A., T. B. Sanford, P. P. Niiler, and E. J. Terrill, 2007: Cold wake of Hurricane Francis. *Geophys. Res. Letters*, **34**, L15609, doi:10.1029/2007GL030160.

Donelan, M. A., B. K. Haus, N. Reul, W. J. Plant, M. Stiassnie, H. C. Graber, O. B. Brown, and E. S. Saltzman, 2004: On the limiting aerodynamic roughness of the ocean in very strong winds. *Geophys. Res. Letters*, **31**, L18306, doi:10.1029/2004GL019460.

Emanuel, K. A., C. DesAutels, C. Holloway, and R. Korty, 2004: environmental controls of tropical cyclone intensity. *J. Atmos. Sci.*, **61**, 843-858.

Fairall, C. W., E. F. Bradley, J. S. Godfrey, G. A. Wick, J. B. Edson, and G. S. Young 1996: Cool-skin and warm-layer effects on sea surface temperature. *J. Geophys. Res*. **101**(C1): doi: 10.1029/95JC03190. issn: 0148-0227.

Halliwell, Jr., G. R., R. H. Weisberg, and D. A. Mayer, 2003: A synthetic float analysis of upper-limb meridional overturning circulation interior ocean pathways in the tropical/subtropical Atlantic. In: *Interhemispheric Water Exchange in the Atlantic Ocean*, G. Goni and P. Malanotte-Rizzoli, editors, Elsevier Publishing Company, 93-136.

Halliwell, Jr., G. R., 2004: Evaluation of vertical coordinate and vertical mixing algorithms in the hybrid-coordinate ocean model (HYCOM). *Ocean Modelling*, **7**, 285-322.

Halliwell Jr. G. R., L. K. Shay, Jacob, O. M. Smedstad, and E. W. Uhlhorn, 2008: Improving ocean model initialization for coupled tropical cyclone forecast models using GODAE nowcasts. *Mon. Wea. Rev*., **136**, 2576-2591.

Halliwell, Jr., G. R., A. Barth, R. H. Weisberg, P. Hogan, O. M. Smedstad, and J. Cummings, 2009: Impact of GODAE products on nested HYCOM simulations of the West Florida Shelf. *Ocean Dyn.*, in press.

Hodur, R. 1997: The Naval Research Laboratory Coupled Ocean/Atmosphere Mesoscale Prediction System (COAMPS). *Mon. Wea. Rev*., *125*, 1414-143.

Hong, X., S. W. Chang, S. Raman, L. K. Shay, and R. Hodur, 2000: The interaction between hurricane Opal (1995) and a warm core ring in the Gulf of Mexico. *Mon. Wea. Rev.*, **128**, 1347-1365.

Jacob, S. D., L. K. Shay, A. J. Mariano, and P. G. Black, 2000: The 3-D oceanic mixed-layer response to Hurricane Gilbert. *J. Phys. Oceanogr.*, **30**, 1407-1429.

Jacob, S. D. and L. K. Shay, 2003: The role of oceanic mesoscale features on the tropical cyclone induced mixed layer response. J. Phys. Oceanogr. 33, 649-676.

Jaimes, B. and L. K. Shay, 2009a: Mixed layer cooling in mesoscale ocean eddies during hurricanes Katrina and Rita. Submitted.

Jaimes, B. and L. K. Shay, 2009b: Near-inertial wave wake of hurricanes Katrina and Rita over mesoscale oceanic eddies. Submitted.

Kara, A. B., P. A. Rochford, and H. E. Hurlburt, 2002: Air-sea flux estimates and the 1997-1998 ENSO event. *Boundary Layer Meteorol.*, **103**, 439-458.

Large, W. and S. Pond, 1981: Open ocean momentum flux measurements in moderate to strong winds. *J. Phys. Oceanogr.,* **11**, 324-336.

Large, W. G., J. C. Mc Williams, and S. C. Doney, 1994: Oceanic vertical mixing: a review and a model with a nonlocal boundary layer parameterization. *Rev. Geophys*., **32**, 363-403.

Leipper, D. F. and D. Volgenau, 1972: Hurricane Heat Potential of the Gulf of Mexico, *J. Phys. Oceanogr.*, **2**, 218-224.

Lin, I-I, C-C. Wu, K. A. Emmanuel, I-H Lee, C-R. Wu, and I-F Pun, 2005: The interaction of supertyphoon Maemi (2003) with a warm ocean eddy. *Mon. Wea. Rev.*, **133**, 2635-2649.

Lin, I-I, C-C Wu, and I-F Pun, 2008: Upper ocean thermal structure and the western North Pacific category 5 typhoons. Part I: Ocean features and the category 5 typhoons' intensification. *Mon. Wea. Rev.*, **136**, 3288-3306.

Mainelli, M., M. DeMaria, L. K. Shay, and G. Goni, 2008: Application of oceanic heat content estimation to operational forecasting of recent category 5 hurricanes. *Wea. And Forecast.*, resubmitted.

Mellor, G. L. and Yamada, T., 1982: Development of a turbulence closure model for geophysical fluid problems. *Rev. Geophys. Space Phys.*, **20**, 851-875.

Murphy, A. H., 1988. Skill scores based on the mean square error and their relationships to the correlation coefficient. *Mon. Wea. Rev.*, **116**, 2417-2424.

Powell, M. D., S. H. Houston, L. R. Amat, and N Morisseau-Leroy, 1998: The HRD real-time hurricane wind analysis system. *J. Wind Engineer. and Indust. Aerodyn*. **78**, 53-64.

Powell, M. D., P. J. Vickery, and T. A. Reinhold, 2003: Reduced drag coefficient for high wind speeds in tropical cyclones. *Nature,* **422**, 279-283.

Reynolds, R. W., N. A. Rayner, T. M. Smith, D. C. Stokes and W. Wang, 2002: An improved in situ and satellite SST analysis for climate. J. Climate, 15, 1609-1625.

Sanford, T. B., J. F. Price, J. B. Girton, and D. C. Webb, 2007: Highly resolved ocean response to a hurricane. *Geophys. Res. Lett.*, **34**, L13604, doi:10.1029/2007GL029679.

Schade, L. R. and K. A. Emanuel, 1999: The ocean's effect on the intensity of tropical cyclones: results from a simple coupled atmosphere-ocean model. *J. Atmos. Sci.*, **56**, 642-651.

Scharroo, R., W. H. Smith, and J. L. Lillibridge, 2005: Satellite altimetry and the intensification of hurricane Katrina. *EOS*, **86**, 366-367.

Shay, L.K., 2008: Upper Ocean Structure: a Revisit of the Response to Strong Forcing Events. In*:Encyclopedia of Ocean Sciences*, ed. John Steele, S.A. Thorpe, Karl Turekian and R. A. Weller, Elsevier Press International, Oxford, UK (Submitted), 19 pp. ***(In Press)***

Shay, L.K. and R.L. Elsberry. 1987: Near-inertial ocean current response to hurricane Frederic. *J. Phys. Oceanogr.*, **17**, 1249 – 1269.

Shay, L.K., R.L. Elsberry and P.G. Black. 1989:Vertical structure of the ocean current response to a hurricane. *J. Phys. Oceanogr.*, **19**, 1249 - 1269.

Shay, L. K., G. J. Goni, and P. G. Black, 2000: Effects of a warm oceanic feature on hurricane Opal. *Mon. Wea. Rev.*, **128**, 1366-1383.

Shay, L. K. and Jacob, S. D., 2006: Relationship between oceanic energy fluxes and surface winds during tropical cyclone passage. Chapter 5, *Atmosphere-Ocean Interactions II, Advances in Fluid Mechanics*. W. Perrie, Ed., WIT Press, Southamption, UK. 115-142.

Shay L. K. and E. W. Uhlhorn, 2008: Loop Current response to hurricanes Isidore and Lili. *Mon. Wea. Rev*., **136**, 3248-3274.

Shen, W., I. Ginis, and R. E. Tuleya, 2002: A numerical investigation of land surface water on landfalling hurricanes. *J. Atmos. Sci.*, **59**, 789-802.

Sun, D., R. Gautam, G. Cervone, Z. Boyeyi, and M. Kaptos, 2006: Comments on satellite altimetry and the intensification of hurricane Katrina. *EOS,*, **87(8)**, 89.

Taylor, K. E., 2001: Summarizing multiple aspects of model performance in a single diagram. *J. Geophys. Re*s., **106**, 7183-7192.

Teague, W. J., E. Jarosz, M. R. Carnes, D. A. Mitchell, and P. J. Hogan, 2006: Low-frequency current variability observed at the shelfbreak in the northeastern Gulf of Mexico: May-October 2004. *Cont. Shelf Res*., **26**, 2559-2582.

Teague, W. J., E. Jarosz, D. W. Wang, and D. A. Mitchell, 2007: Observed oceanic response over the upper continental slope and outer shelf during Hurricane Ivan, *J. Phys. Oceanogr.* **37**, 2181-2206.

Wada, A. and N. Usui, 2007: Importance of tropical cyclone heat potential for tropical cyclone intensity and intensification in the western North Pacific. *J. Oceanogr.*, **63**, 427-447.

Walker, N., R. R. Leben, and S. Balasubramanian, 2005: Hurricane forced upwelling and chlorophyll a enhancement within cold core cyclones in the Gulf of Mexico. *Geophys. Res. Lett.*, **32**, L18610, doi: 10.1029/2005GL023716, 1-5.

Wu, L., B. Wang, and S. A. Braun, 2005: Impacts of air-sea interaction on tropical cyclone track and intensity. *Mon. Wea. Rev.*, **133**, 3299-3314.

Wu, C-C, C-Y Lee, and I-I Lin, 2007: The effect of the ocean eddy on tropical cyclone intensity. *J. Atmos. Sci.*, **64**, 3562-3578.

Figure Captions

Figure 1. SSH maps for 00 UTC, 10 Sept. 2004 from initial model fields provided by a data-assimilative GOM hindcast for experiments GOM1-GOM12 (top), and provided by a non-assimilative GOM simulation for experiment GOM13 (bottom). The red arrows point to the two cold-core cyclones where Ivan forced large cooling.

Figure 2. Map of 10 m wind speed in the eastern GOM on 15 Sept. from the blended COAMPS-H*WIND forcing product. The white circle illustrates the radius of maximum wind R_{MAX}=45km. The magenta circle ($1.4R_{MAX}$) and black circle ($3.0R_{MAX}$) illustrate the averaging domains for the air-sea thermal heat flux sensitivity analysis in Figure 10.

Figure 3. Upper-ocean zonal cross-sections of initial (00 UTC, 10 Sept. 2004) ocean temperature fields provided by the data-assimilative GOM hindcast for the three different vertical resolutions tested: low resolution used for GOM3 (top), high resolution used for GOM4 (bottom), and medium resolution used for all other experiments. The fixed coordinates near the surface follow the HYCOM convention of increasing thickness with depth until a prescribed maximum thickness is reached. The range of layer thickness for each experiment is listed in Table 1.

Figure 4. The wind stress drag coefficients C_D as a function of wind speed (top), and the latent and sensible heat flux coefficients C_{EL} and C_{ES} as a function of wind speed (bottom)

provided to model experiments. The five wind stress drag coefficients are Donelan (black), Powell (red), Large and Pond (green), Large & Pond capped (blue above 30 ms^{-1}), and Shay and Jacob (magenta). The Shay and Jacob algorithm reverts to Large and Pond below 10 m s^{-1} wind speed. The heat flux coefficients are the COARE3.0 algorithm (C_{EL}, black solid; C_{ES}, black dashed) and Kara *et al.* (C_{EL}, red solid; C_{ES}, red dashed), and are calculated assuming an air temperature of 27°C and a SST of 29°C. Similar differences between these two algorithms are realized for different choices of air temperature and SST.

Figure 5. Map of sea surface height (top panel) on 17 Sept. 2004 shortly after Ivan made landfall (track in black line), illustrating the locations of the LC, the detached warm ring, and the two cyclonic eddies (red arrows) near the time of maximum cooling in the eastern GoM. A white dot marks the location of SEED ADCP mooring 9 (Teague *et al.*, 2007) while the other two unmarked white dots represent the locations sampled by synthetic instruments and described in Figure 6. The remaining panels present SST maps for 10 Sept. 2004 (left) and 17 Sept. 2004 (right) for the Reynolds blended analysis of *in-situ* observations plus infrared and microwave satellite data (top) and from the control experiment GOM1 (bottom).

Figure 6. Time series of temperature over the upper 400 m (top row), and of the three terms of Equation (1) (second row), at a location in the detached warm ring. Also shown are the same two plots at a location in the southern cold-core cyclone (bottom two rows). The left panels are for the control experiment GOM1 while the right panels are for the one-dimensional experiment GOM14. These locations are illustrated by white dots in the top panel of Figure 5. The thick black line denotes the OML base diagnosed as the depth where temperature reaches 0.5°C below SST. The magenta line follows the 20°C isotherm in the depth-time temperature plots. For the terms of Equation (1), w_E is the black line, w_M is the blue line, and $\partial z_M/\partial t$ is the red line.

Figure 7. Sensitivity analysis of SST change forced by hurricane Ivan (track in black line), as summarized by differences in the SST change (Sept. 17 minus Sept. 11) calculated using Equation (2)between the control experiment GOM1 and each of the remaining experiments

GOM2-GOM14. The RMS amplitude of ΔT (°C), which represents the RMS difference between the SST changes forced by the two experiments, are tabulated in the third column. Four ΔT maps are shown as examples. All RMS ΔT values are calculated within the rectangular boxes outlined by black lines in the maps (extreme NW Caribbean Sea and eastern GoM).

Figure 8. Taylor diagram comparing ΔT calculated using (Equation number) from the control experiment to ΔT from all remaining experiments. Symbols representing the different experiments are labeled in the Legend. Different symbol colors in the diagram and in the Legend categorize the individual model attributes that are varied: horizontal and vertical resolution (red), vertical mixing choice (green), wind stress drag coefficient (blue), turbulent heat flux coefficient (cyan), atmospheric forcing resolution (magenta) and outer model choice (yellow). The large black square at a correlation of 1.0 and RMS amplitude of 1.0 represents a perfect comparison.

Figure 9. Taylor diagram comparing ΔT calculated from Equation (2) for each experiment to observed ΔT estimated from the Reynolds SST analysis. Symbols and colors follow the conventions used in Figure 8 except that the control experiment is included as a black circle. The large black square represents a perfect comparison.

Figure 10. Air sea thermal heat flux averaged over $1.4R_{MAX}$ (left panels) and $3.0R_{MAX}$ (right panels) following the path of the storm and graphed as a function of storm central latitude. In each panel, the control experiment is compared to alternate experiments representing a particular category of model attribute being varied: model resolution (top row), vertical mixing choice (second row), wind stress drag coefficient (third row), turbulent heat flux drag coefficients (fourth row), and both surface forcing resolution and the outer model used for nesting (bottom row). The control experiment is represented by the black line in all panels. Colors representing other experiments are shown in the legends at right. Negative values indicate heat flux from ocean to atmosphere.

Figure 11. Time series of *w* at a location in the eastern part of the southern cold cyclone (left panels) and at the eastern side of the warm ring (right panels) at the two locations shown in the top panel of Figure 5. The experiments are sorted into separate panels based on the type of model attribute as in Figure 10. The control experiment is represented by the black line in all panels. Colors representing other experiments are shown in the legends at right.

Figure 12. Time series of *u* and *v* over the upper 150 m at SEED mooring 9 from observations (top panels) and the control experiment GOM1 (bottom panels). The time axis has been scaled to local inertial period from the time of closest approach of the storm center.

Figure 13. Taylor diagram comparing the simulated north-south (cross-shelf and along-track) velocity component from the control experiment from the upper 150 m shown in Figure 11 to the same field from all remaining experiments. Symbols and colors follow the conventions used in Figure 8. The large black square represents a perfect comparison.

Figure 14. Taylor diagram comparing the simulated north-south (cross-shelf and along-track) velocity component for each experiment to the same field from the ADCP observations. Symbols and colors follow the conventions used in Figure 7. The large black square represents a perfect comparison.

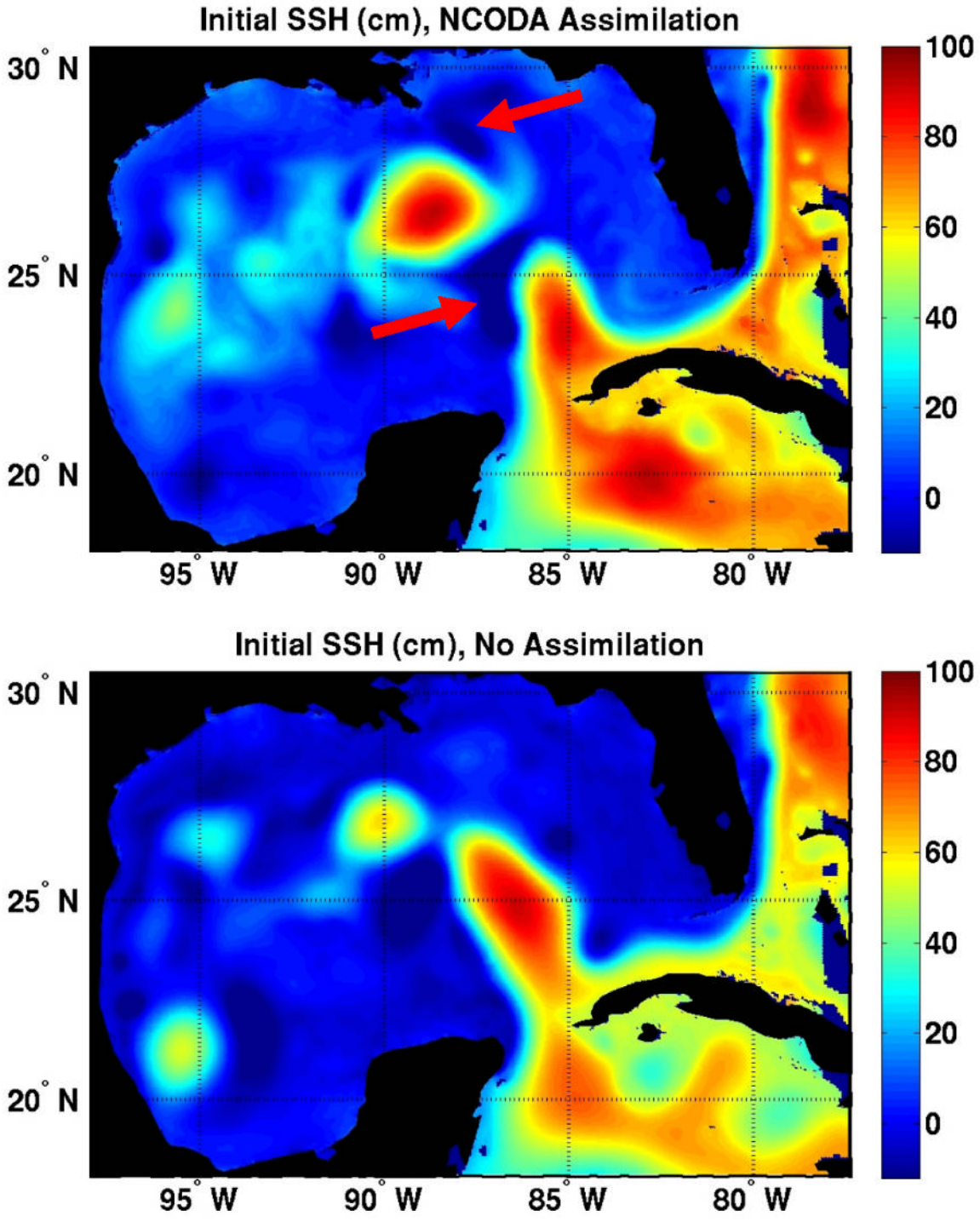

Figure 1. SSH maps for 00 UTC, 10 Sept. 2004 from initial model fields provided by a data-assimilative GOM hindcast for experiments GOM1-GOM12 (top), and provided by a non-assimilative GOM simulation for experiment GOM13 (bottom). The red arrows point to the two cold-core cyclones where Ivan forced large cooling.

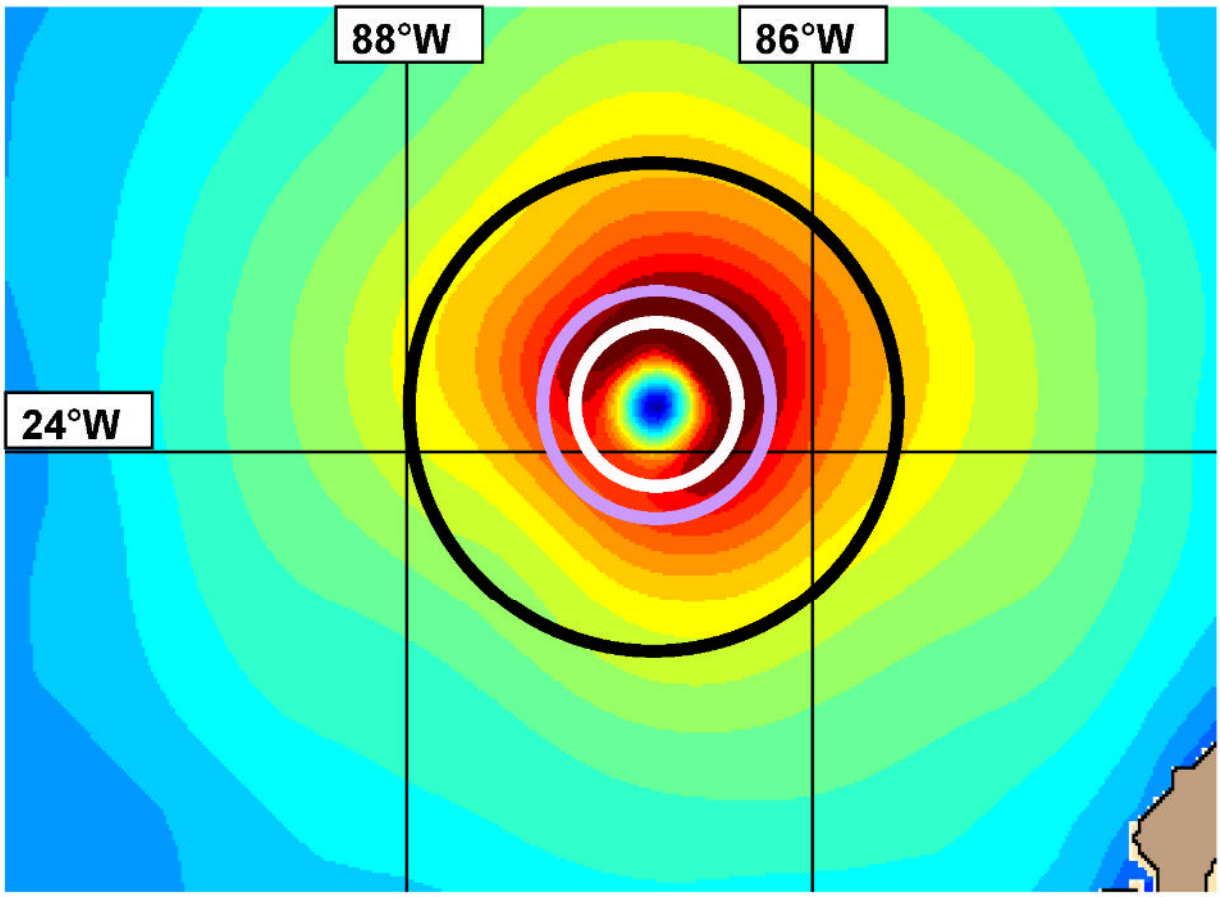

Figure 2. Map of 10 m wind speed in the eastern GOM on 15 Sept. from the blended COAMPS-H*WIND forcing product. The white circle illustrates the radius of maximum wind R_{MAX}=45km. The magenta circle ($1.4R_{MAX}$) and black circle ($3.0R_{MAX}$) illustrate the averaging domains for the air-sea thermal heat flux sensitivity analysis in Figure 10.

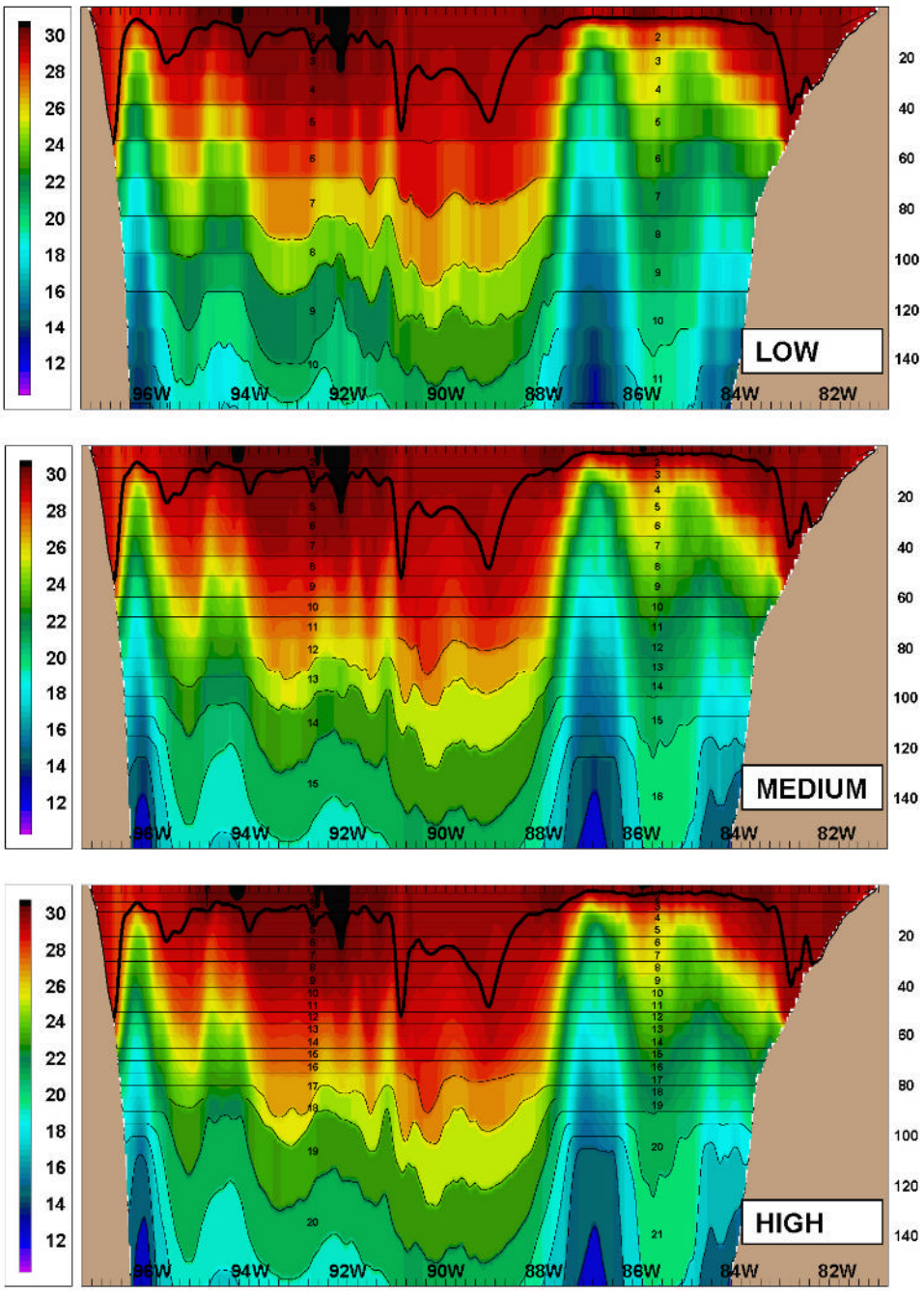

Figure 3. Upper-ocean zonal cross-sections of initial (00 UTC, 10 Sept. 2004) ocean temperature fields provided by the data-assimilative GOM hindcast for the three different vertical resolutions tested: low resolution used for GOM3 (top), high resolution used for GOM4 (bottom), and medium resolution used for all other experiments. The fixed coordinates near the surface follow the HYCOM convention of increasing thickness with depth until a prescribed maximum thickness is reached. The range of layer thickness for each experiment is listed in Table 1.

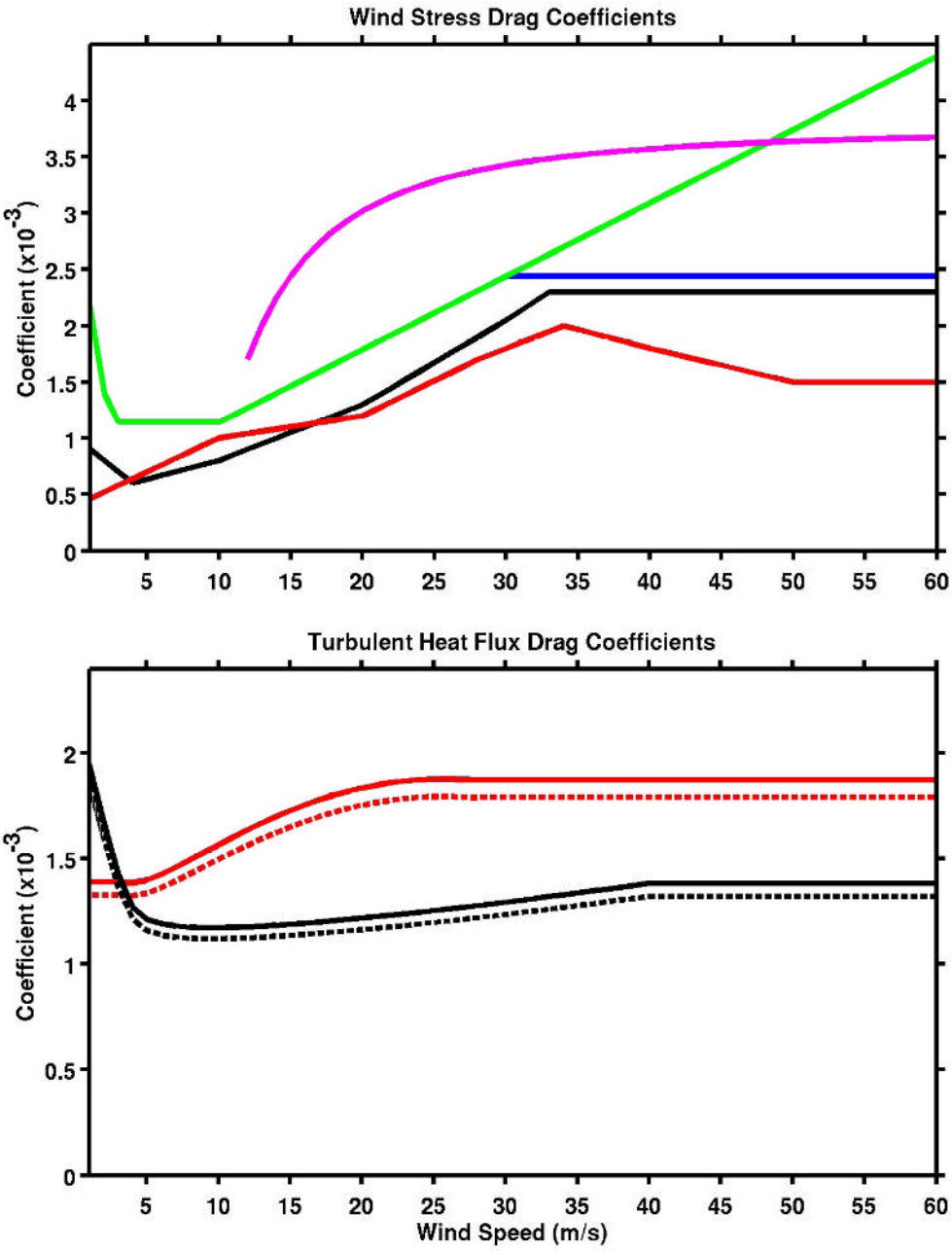

Figure 4. The wind stress drag coefficients C_D as a function of wind speed (top), and the latent and sensible heat flux coefficients C_{EL} and C_{ES} as a function of wind speed (bottom) provided to model experiments. The five wind stress drag coefficients are Donelan (black), Powell (red), Large and Pond (green), Large & Pond capped (blue above 30 ms^{-1}), and Shay and Jacob (magenta). The Shay and Jacob algorithm reverts to Large and Pond below 10 m s^{-1} wind speed. The heat flux coefficients are the COARE3.0 algorithm (C_{EL}, black solid; C_{ES}, black dashed) and Kara *et al.* (C_{EL}, red solid; C_{ES}, red dashed), and are calculated assuming an air temperature of 27°C and a SST of 29°C. Similar differences between these two algorithms are realized for different choices of air temperature and SST.

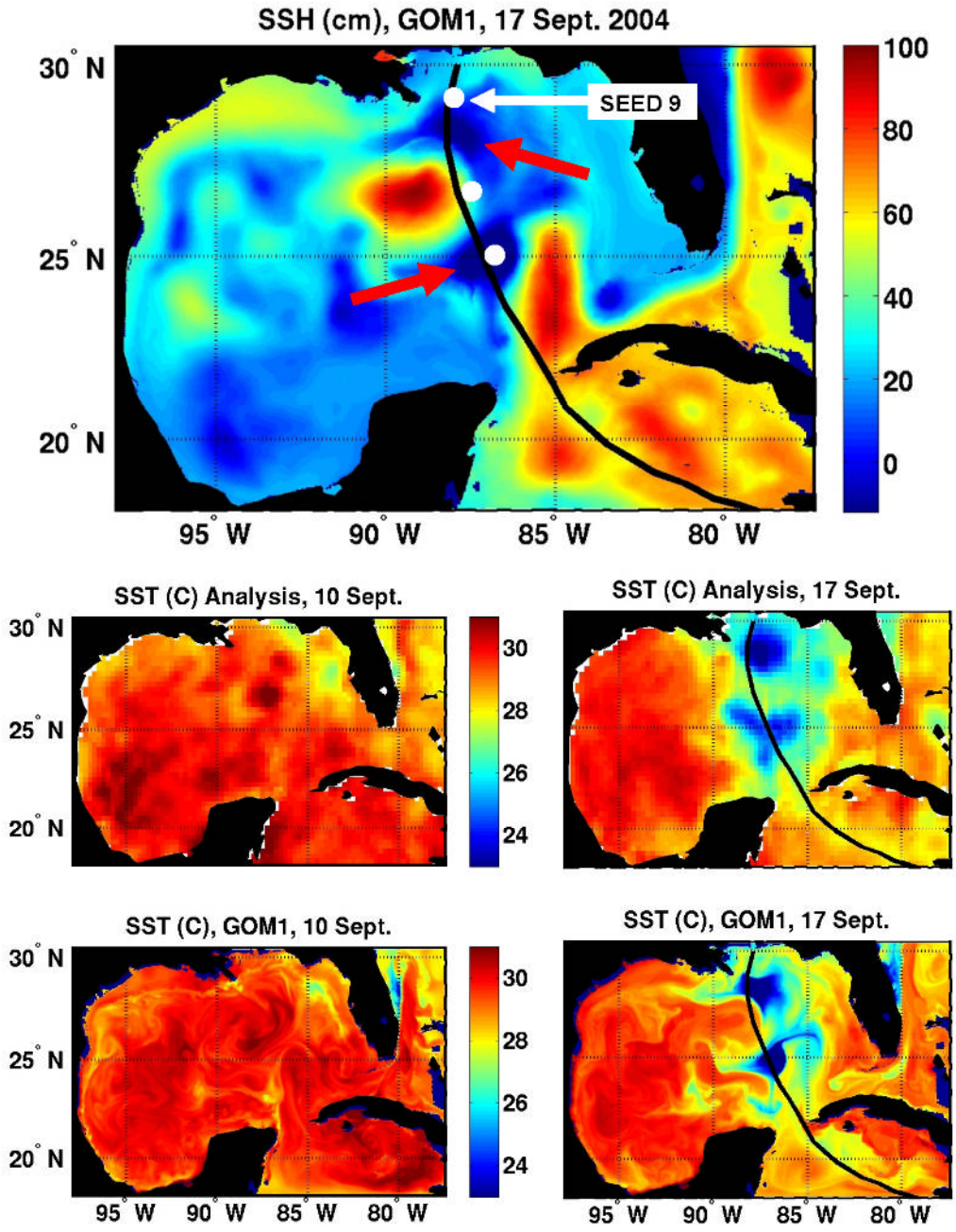

Figure 5. Map of sea surface height (top panel) on 17 Sept. 2004 shortly after Ivan made landfall (track in black line), illustrating the locations of the LC, the detached warm ring, and the two cyclonic eddies (red arrows) near the time of maximum cooling in the eastern GoM. A white dot marks the location of SEED ADCP mooring 9 (Teague *et al.*, 2007) while the other two unmarked white dots represent the locations sampled by synthetic instruments and described in Figure 6. The remaining panels present SST maps for 10 Sept. 2004 (left) and 17 Sept. 2004 (right) for the Reynolds blended analysis of *in-situ* observations plus infrared and microwave satellite data (top) and from the control experiment GOM1 (bottom).

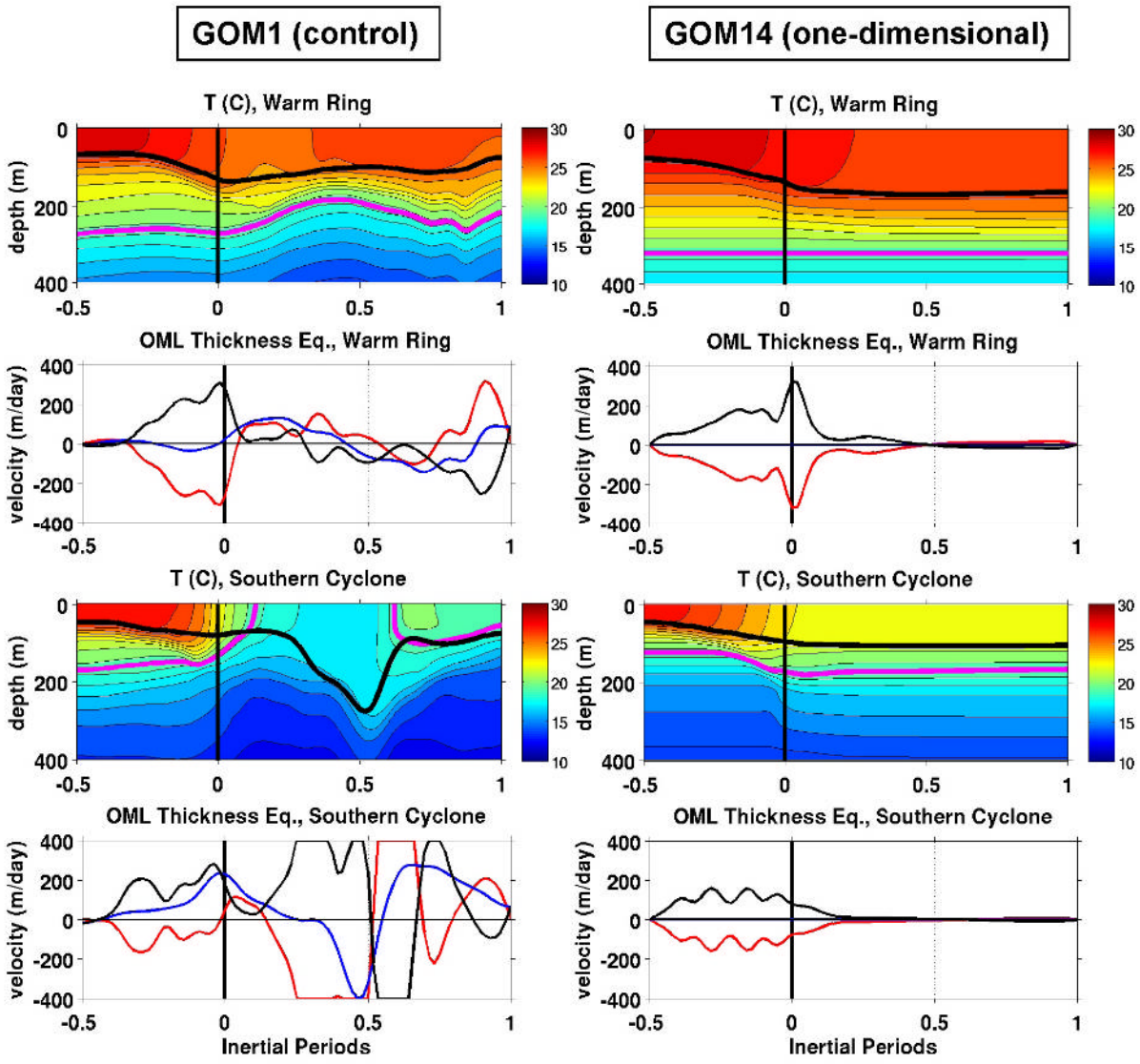

Figure 6. Time series of temperature over the upper 400 m (top row), and of the three terms of Equation (1) (second row), at a location in the detached warm ring. Also shown are the same two plots at a location in the southern cold-core cyclone (bottom two rows). The left panels are for the control experiment GOM1 while the right panels are for the one-dimensional experiment GOM14. These locations are illustrated by white dots in the top panel of Figure 5. The thick black line denotes the OML base diagnosed as the depth where temperature reaches 0.5°C below SST. The magenta line follows the 20°C isotherm in the depth-time temperature plots. For the terms of Equation (1), w_E is the black line, w_M is the blue line, and $\partial z_M/\partial t$ is the red line.

Alternate Experiment	Model Attribute	ΔT (C) Mean Diff.	ΔT (C) RMS
GOM2	Low horiz. res.	+0.01	0.47
GOM3	Low vert. res.	+0.05	0.29
GOM4	High vert. res.	-0.02	0.26
GOM5	MY mixing	+0.06	0.49
GOM6	GISS mixing	+0.21	0.37
GOM7	Powell C_D	+0.13	0.33
GOM8	Large&Pond C_D	-0.19	0.48
GOM9	Large&Pond (capped) C_D	-0.08	0.19
GOM10	Shay&Jacob C_D	-0.39	0.75
GOM11	Kara et al. C_L, C_S	-0.13	0.18
GOM12	No H*WIND	+0.25	0.70
GOM13	Outer model	+0.43	1.57
GOM14	One-dimensional	-0.17	1.31

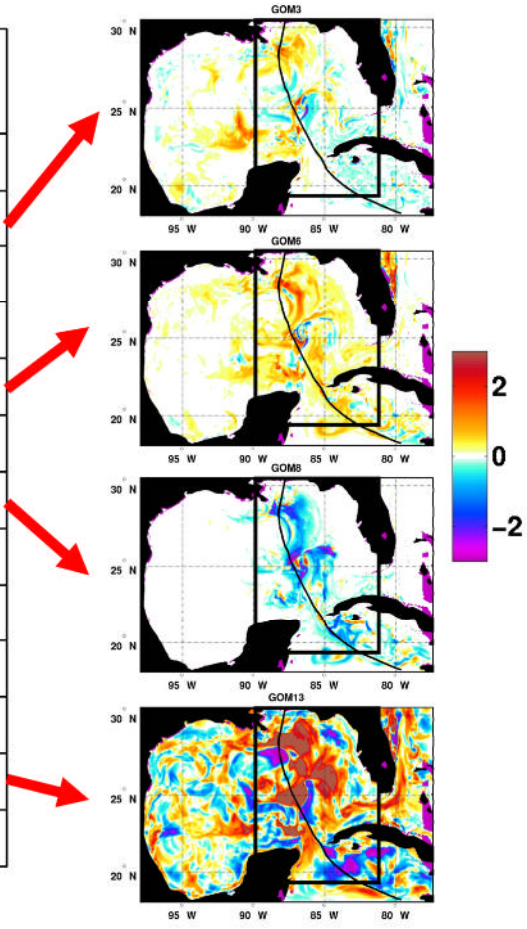

Figure 7. Sensitivity analysis of SST change forced by hurricane Ivan (track in black line), as summarized by differences in the SST change (Sept. 17 minus Sept. 11) calculated using Equation (2)between the control experiment GOM1 and each of the remaining experiments GOM2-GOM14. The RMS amplitude of ΔT (°C), which represents the RMS difference between the SST changes forced by the two experiments, are tabulated in the third column. Four ΔT maps are shown as examples. All RMS ΔT values are calculated within the rectangular boxes outlined by black lines in the maps (extreme NW Caribbean Sea and eastern GoM).

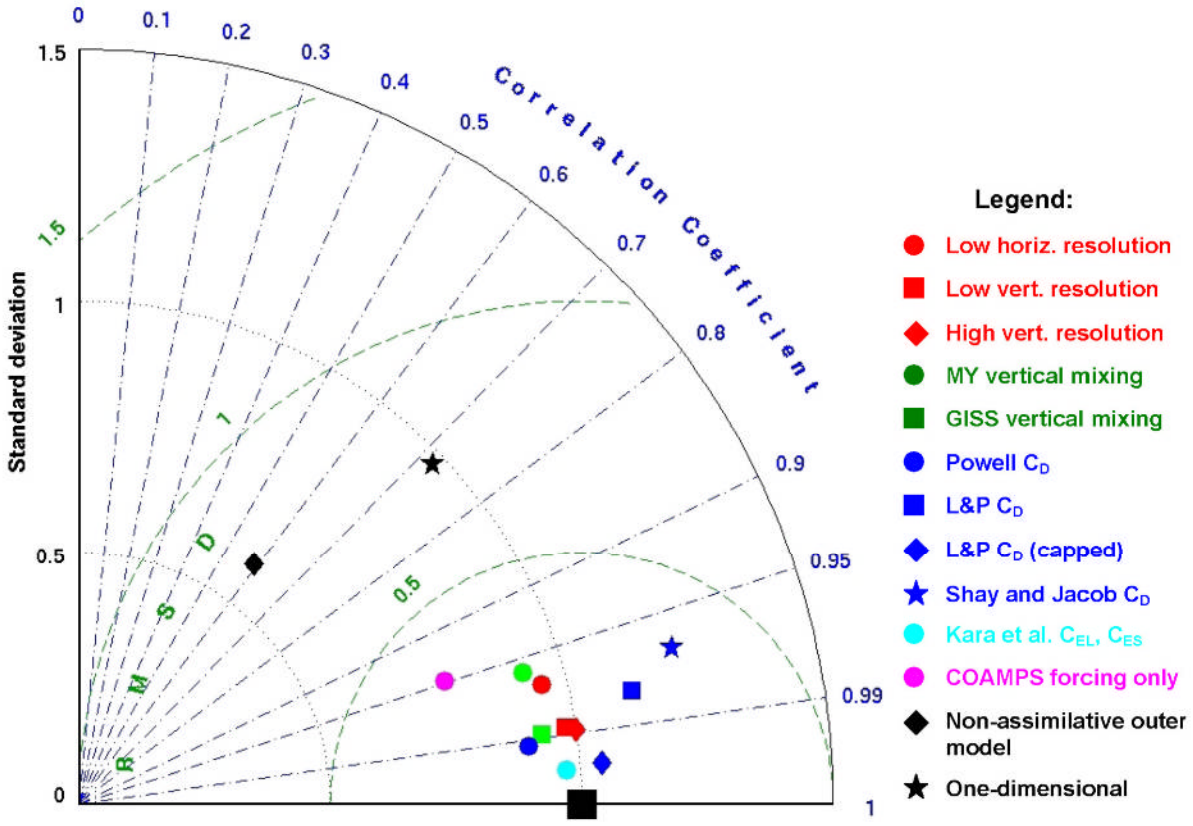

Figure 8. Taylor diagram comparing ΔT calculated using (Equation number) from the control experiment to ΔT from all remaining experiments. Symbols representing the different experiments are labeled in the Legend. Different symbol colors in the diagram and in the Legend categorize the individual model attributes that are varied: horizontal and vertical resolution (red), vertical mixing choice (green), wind stress drag coefficient (blue), turbulent heat flux coefficient (cyan), atmospheric forcing resolution (magenta) and outer model choice (yellow). The large black square at a correlation of 1.0 and RMS amplitude of 1.0 represents a perfect comparison.

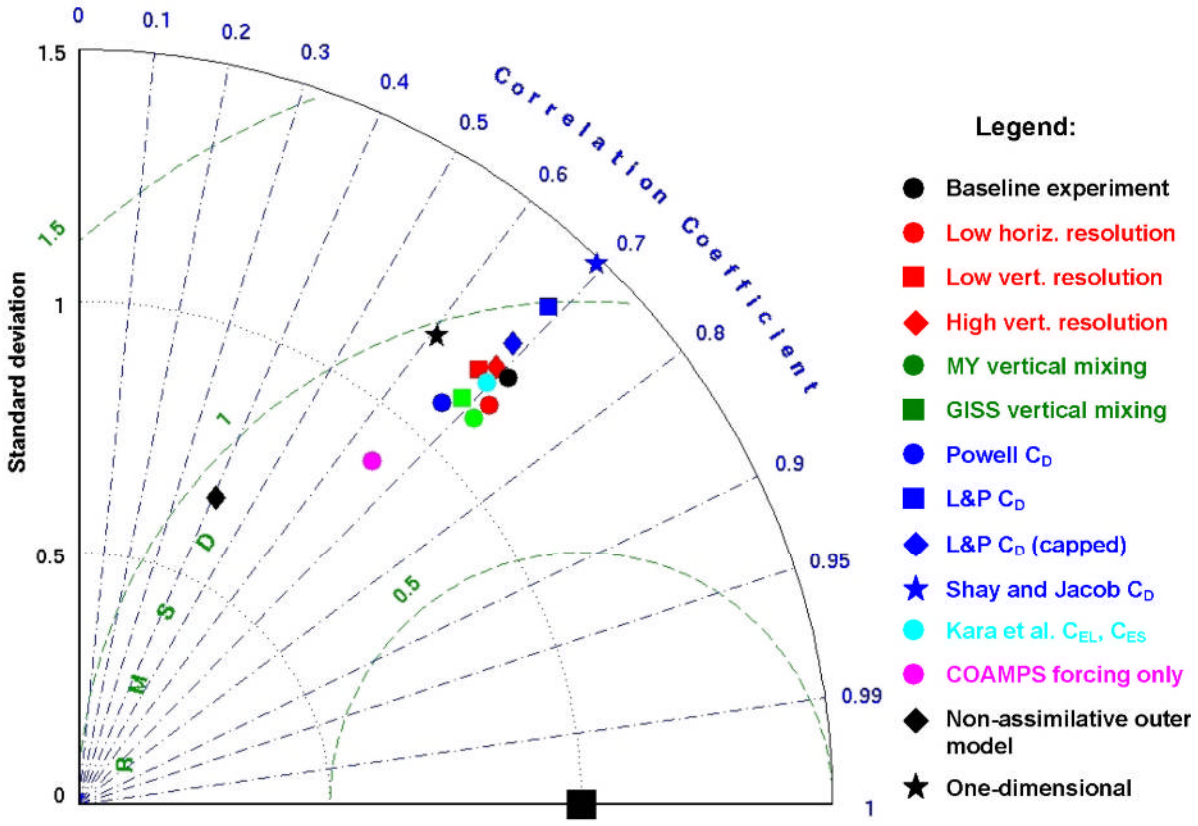

Figure 9. Taylor diagram comparing ΔT calculated from Equation (2) for each experiment to observed ΔT estimated from the Reynolds SST analysis. Symbols and colors follow the conventions used in Figure 8 except that the control experiment is included as a black circle. The large black square represents a perfect comparison.

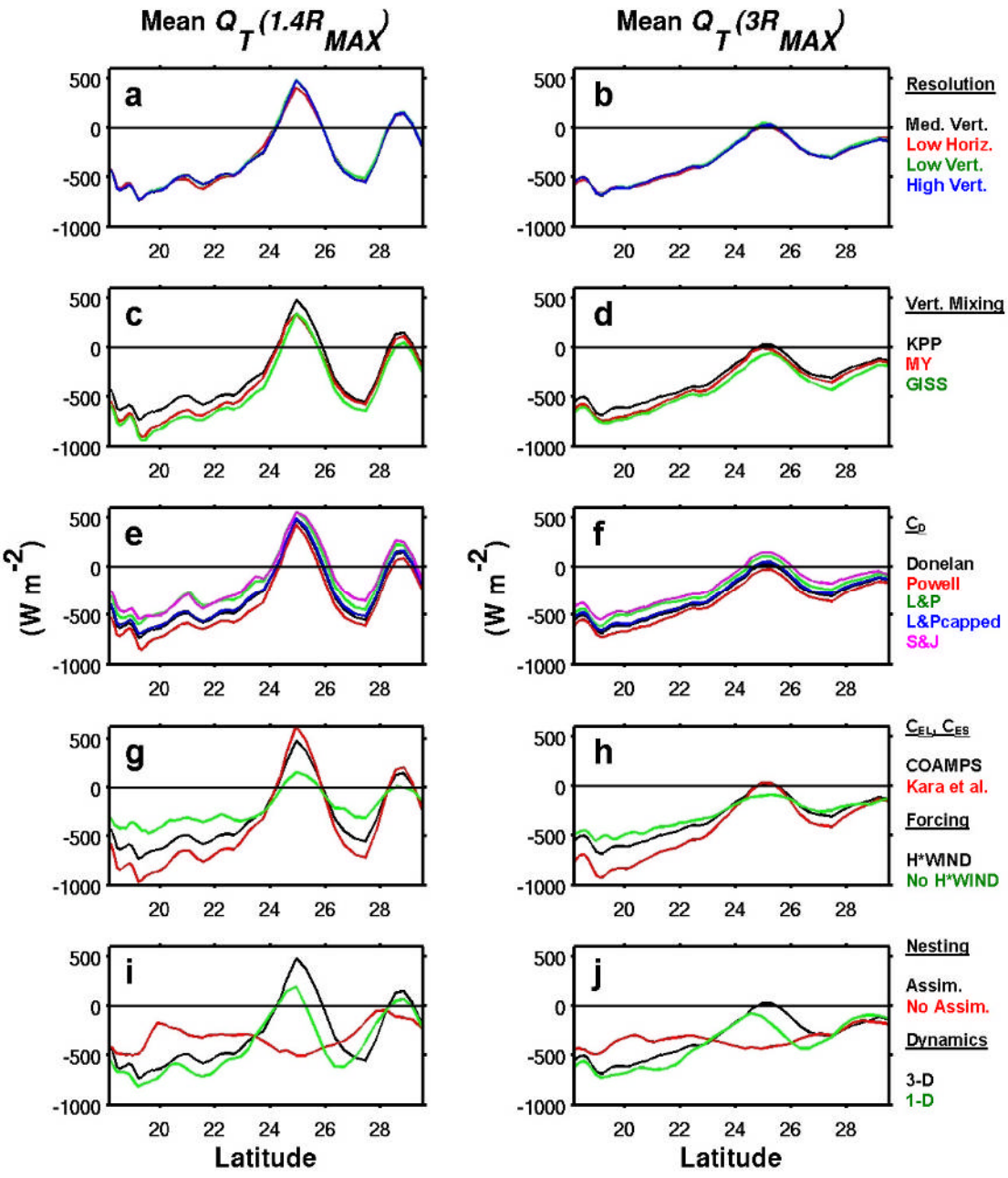

Figure 10. Air sea thermal heat flux averaged over $1.4R_{MAX}$ (left panels) and $3.0R_{MAX}$ (right panels) following the path of the storm and graphed as a function of storm central latitude. In each panel, the control experiment is compared to alternate experiments representing a particular category of model attribute being varied: model resolution (top row), vertical mixing choice (second row), wind stress drag coefficient (third row), turbulent heat flux drag coefficients (fourth row), and both surface forcing resolution and the outer model used for nesting (bottom row). The control experiment is represented by the black line in all panels. Colors representing other experiments are shown in the legends at right. Negative values indicate heat flux from ocean to atmosphere.

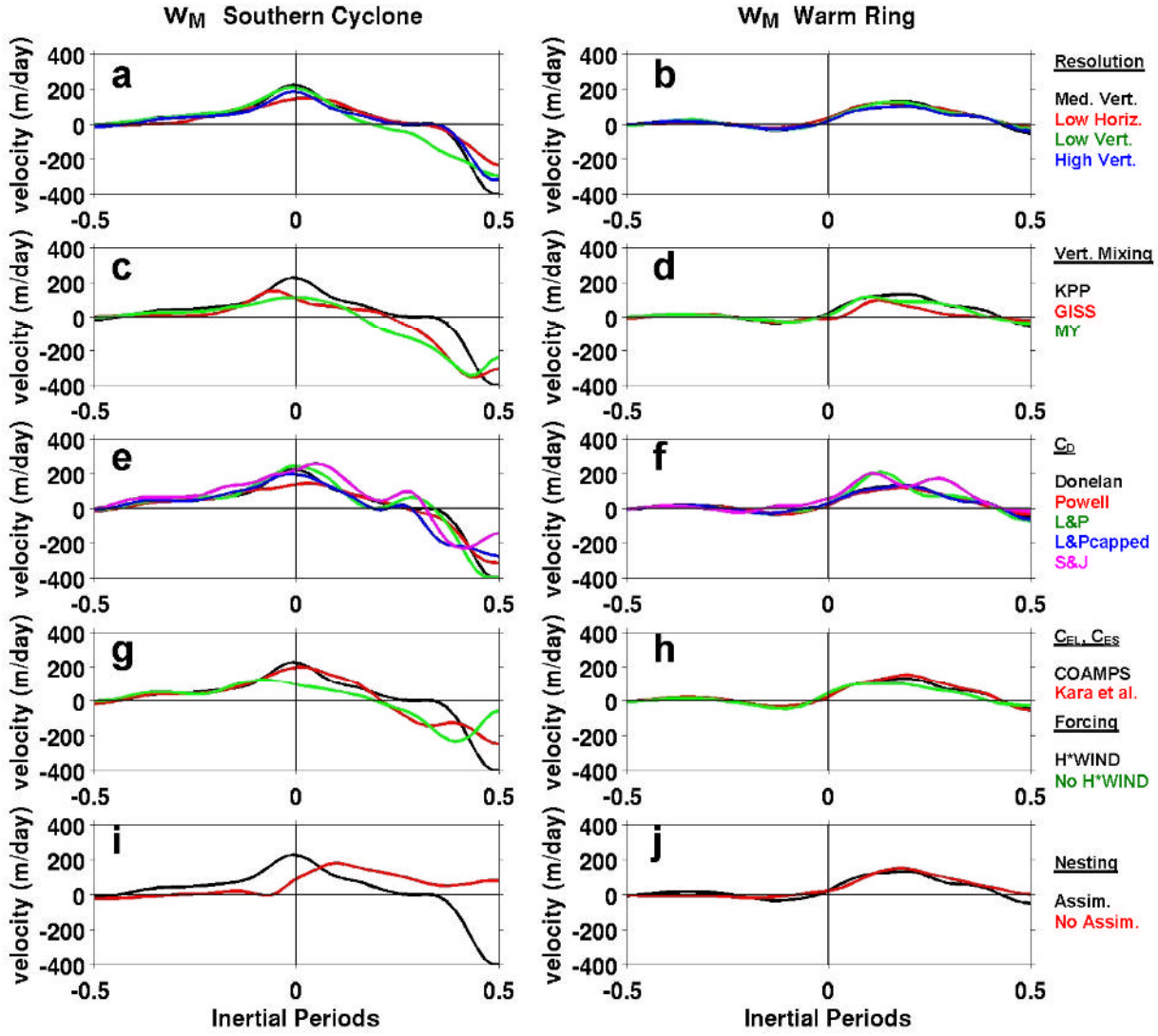

Figure 11. Time series of *w* at a location in the eastern part of the southern cold cyclone (left panels) and at the eastern side of the warm ring (right panels) at the two locations shown in the top panel of Figure 5. The experiments are sorted into separate panels based on the type of model attribute as in Figure 10. The control experiment is represented by the black line in all panels. Colors representing other experiments are shown in the legends at right.

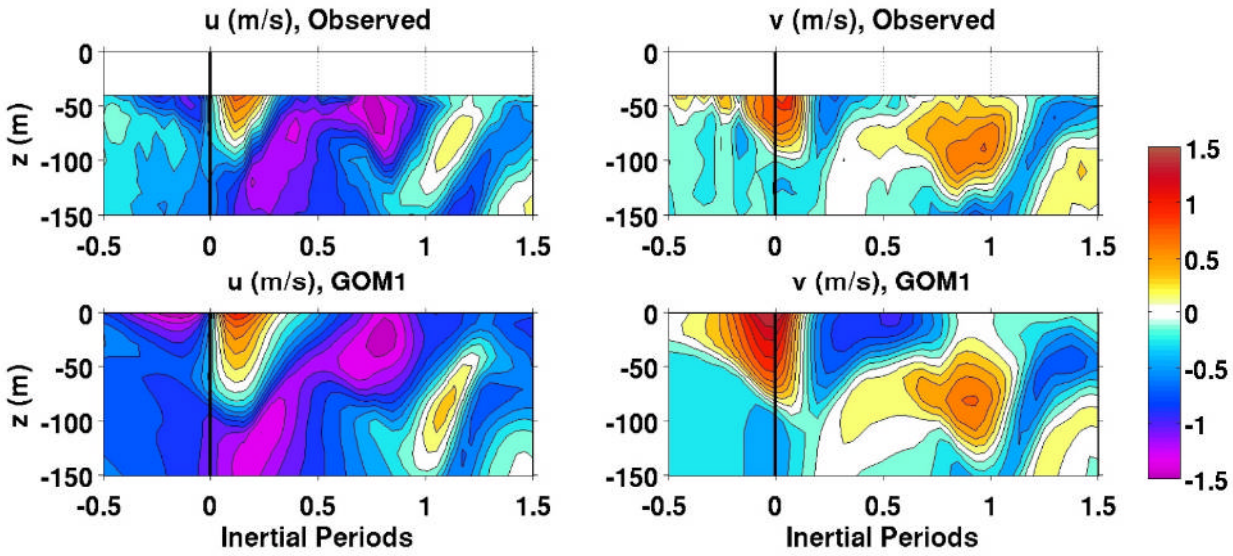

Figure 12. Time series of *u* and *v* over the upper 150 m at SEED mooring 9 from observations (top panels) and the control experiment GOM1 (bottom panels). The time axis has been scaled to local inertial period from the time of closest approach of the storm center.

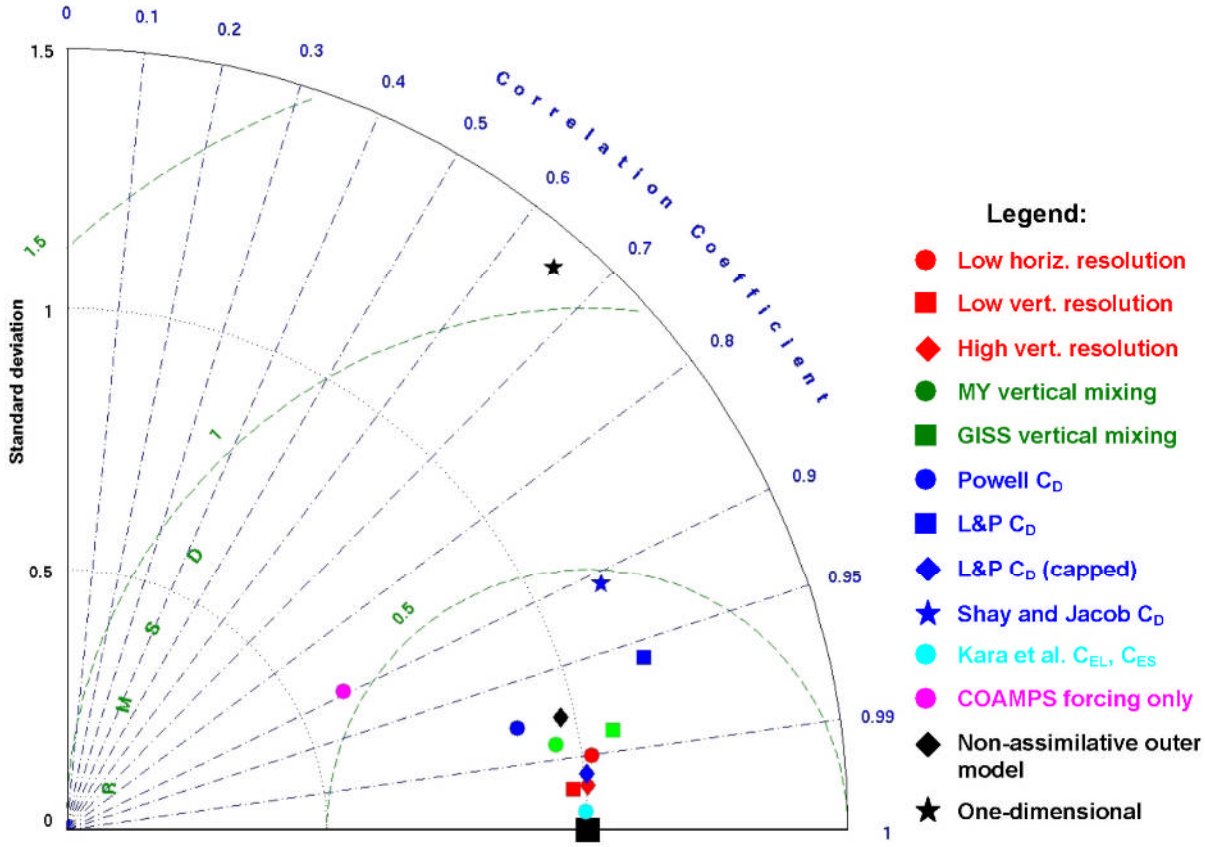

Figure 13. Taylor diagram comparing the simulated north-south (cross-shelf and along-track) velocity component from the control experiment from the upper 150 m shown in Figure 11 to the same field from all remaining experiments. Symbols and colors follow the conventions used in Figure 8. The large black square represents a perfect comparison.

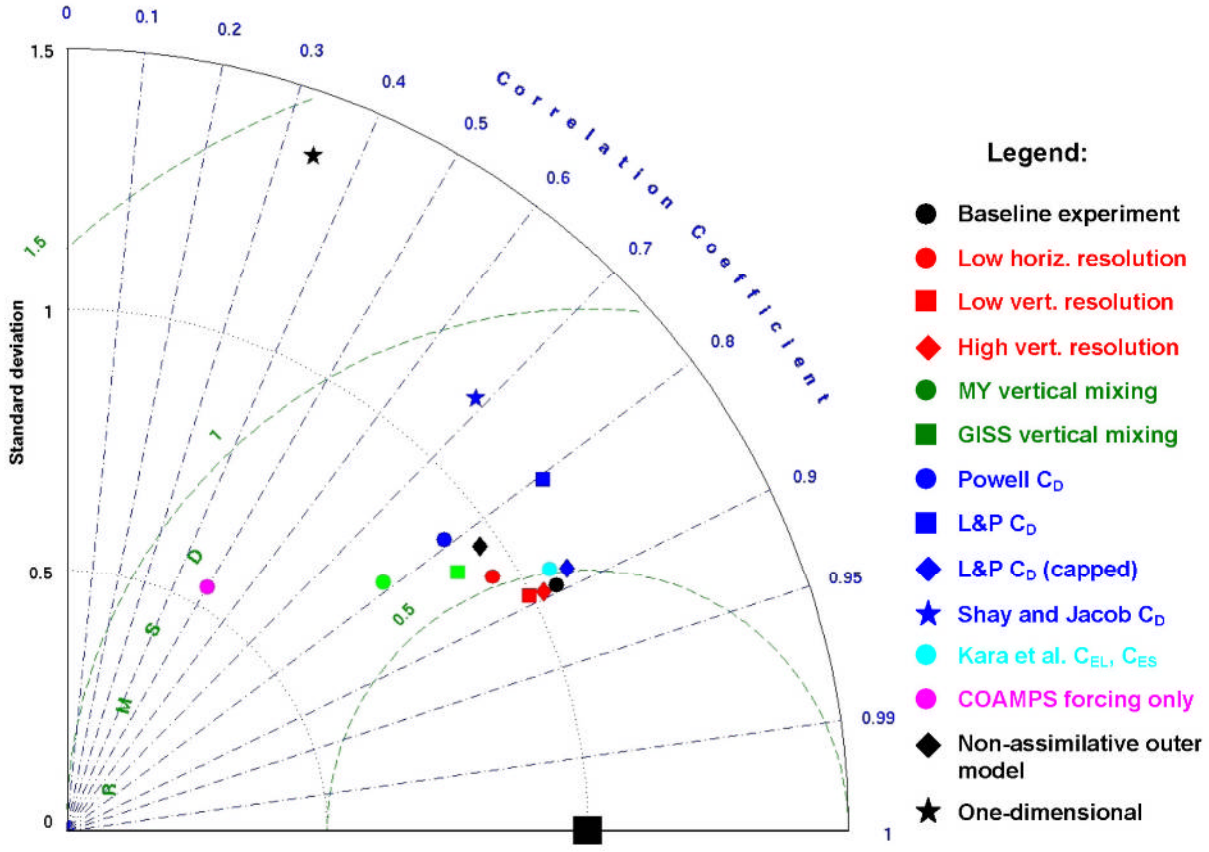

Figure 14. Taylor diagram comparing the simulated north-south (cross-shelf and along-track) velocity component for each experiment to the same field from the ADCP observations. Symbols and colors follow the conventions used in Figure 7. The large black square represents a perfect comparison.

Table 1. Summary of model simulations. The left column lists model attributes while the central column lists the specific attributes of the control experiment GOM1. The right column lists all of the alternate experiments along with the new attribute.

Model Attribute	Control Experiment GOM1	Alternate Experiments
Horizontal resolution	0.04° Mercator	**GOM2**: 0.08° Mercator
Vertical resolution	26 layers, 4-8m in OML	**GOM3**: 21 layers, 7.5-15m in OML **GOM4**: 31 layers, 3-5m in OML
Vertical mixing	KPP	**GOM5**: MY **GOM6**: GISS
C_D	Donelan	**GOM7**: Powell **GOM8**: Large and Pond **GOM9**: Large and Pond (capped) **GOM10**: Shay and Jacob
C_{EL}, C_{ES}	COARE3.0 algorithm	**GOM11**: Kara *et al.*
Atmospheric forcing	27-km COAMPS+H*WIND	**GOM12**: 27-km COAMPS only
Outer model	NCODA GOM hindcast	**GOM13**: Free GOM simulation
Ocean dynamics	Three-dimensional	**GOM14**: One-dimensional

Table 2. Post-Ivan SST (°C) on 17 Sept. 2004 within the northern and southern cold-core cyclones where the largest cooling occurred from both observations and the 13 experiments along with SST differences between each experiment and the observations. SST values were calculated by averaging over 1° by 1° boxes centered at 87.4°W, 28.4°N (northern cyclone) and 86.8°W, 25.0°N (southern cyclone).

Source	Northern Cold-Core Cyclone			Southern Cold-Core Cyclone		
	SST (°C)	Difference From GOM1	Difference From Obs.	SST (°C)	Difference From GOM1	Difference From Obs.
Observations	22.3			23.9		
GOM1	21.7		-0.6	19.6		-4.3
GOM2	21.6	-0.1	-0.7	19.5	-0.1	-4.4
GOM3	21.8	+0.1	-0.5	19.3	-0.3	-4.6
GOM4	21.6	-0.1	-0.7	20.1	+0.5	-3.8
GOM5	22.3	+0.6	0.0	21.4	+1.8	-2.5
GOM6	22.5	+0.8	+0.2	20.2	+0.6	-3.7
GOM7	22.6	+0.9	+0.3	20.5	+0.9	-3.4
GOM8	20.7	-1.0	-1.6	19.0	-0.6	-4.9
GOM9	21.5	-0.2	-0.8	19.2	-0.4	-4.7
GOM10	20.2	-1.5	-2.1	18.1	-1.5	-5.8
GOM11	21.7	0.0	-0.6	19.7	+0.1	-4.2
GOM12	23.7	+2.0	+1.4	22.0	+2.4	-1.9
GOM13	23.4	+1.7	+1.1	26.5	+6.9	+2.6
GOM14	22.7	+1.0	+0.4	22.8	+3.2	-1.1

Table 3. Murphy skill scores *S* from Equation (3) between the 13 experiments and observations for ΔT maps (17 Sept. minus 10 Sept.) calculated from the daily Reynolds SST maps, and also for *u* and *v* profiles measured at SEED mooring 9.

Experiment	ΔT Maps	*u(z,t)*	*v(z,t)*
GOM1	0.21	0.64	0.74
GOM2	0.26	0.65	0.73
GOM3	0.17	0.65	0.75
GOM4	0.16	0.65	0.76
GOM5	0.28	0.61	0.62
GOM6	0.22	0.65	0.69
GOM7	0.22	0.50	0.61
GOM8	-0.05	0.58	0.54
GOM9	0.08	0.62	0.75
GOM10	-0.21	0.55	0.26
GOM11	0.20	0.59	0.74
GOM12	-0.04	0.33	0.25
GOM13	-0.20	0.62	0.66
GOM14	0.01	-1.87	-0.98

Table 4. Summary of the impact of changes in different model attributes on the SST response pattern, the heat flux from ocean to atmosphere, the wind-driven upwelling, and the upper-ocean near-inertial momentum response. Heat flux differences are for the flux averaged over $1.4R_{MAX}$. Sensitivity is measured relative to the control experiment. If the sensitivity depends on location relative to energetic ocean features, the impact on sensitivity is modified by the word "potentially" to indicate that this level of sensitivity may not be true everywhere.

Model Attribute	SST Response Sensitivity (RMS difference from control expt.)	Heat Flux Sensitivity (difference from control expt.)	Upwelling Sensitivity (difference from control expt.)	Upper-Ocean Momentum Sensitivity at SEED 9)	Recommenda-tions
Horizontal resolution	Intermediate (0.47°C)	Low (<10 W m^{-2})	Intermediate (<50 m d^{-1} or <25%)	Low	≈10 km is adequate
Vertical resolution	Low (0.26-0.29°C)	Low (<10 W m^{-2})	Low (<10 m d^{-1} or <5%)	Low	≈10 m in the OML is adequate
Vertical mixing	Intermediate (0.37-0.49°C)	High (<250 W m^{-2})	High (<120 m d^{-1} or <60%)	Intermediate	KPP is a good choice MY, GISS give slower cooling, larger heat flux
C_D	High (up to 0.75°C)	High (<350 W m^{-2})	High (<100 m d^{-1} or <50%)	High (large C_D increases strength and penetration of forced currents)	Donelan, Large & Pond capped are reasonable choices (2.3-2.5 x 10^{-3} at high wind speed)
C_{EL}, C_{ES}	Low (0.18°C)	High (<300 W m^{-2})	Low (<20 m d^{-1} or <10%)	Very low	Default COARE algorithm in HYCOM is a reasonable choice
Atmos-pheric forcing	High (0.70°C)	High (<250 W m^{-2})	High (<140 m d^{-1} or <70%)	Very high	Must resolve inner-core structure (≤10 km resolution)
Outer model	Potentially very high (1.57°C)	Potentially very high (<900 W m^{-2})	Potentially very high (<160 m d^{-1} or <80%)	Intermediate (potentially very high near energetic ocean features)	Accurate initialization critically important
Ocean dynamics	Potentially very high (1.31°C)	Potentially high (<300 W m^{-2})	Zero upwelling in 1-D experiment	Very high (pure inertial response)	Ocean model must resolve 3-D ocean dynamics